TITLE OF MY THESIS

Inauguraldissertation
der Philosophisch-naturwissenschaftlichen Fakultät
der Universität Bern

vorgelegt von

MARIA IAKOVLEVA

von St.Petersburg

Leiter der Arbeit:

Prof. Dr. Peter Wurz

Physics Institute
Space Research and Planetary Sciences

TITLE OF MY THESIS

Inauguraldissertation
der Philosophisch-naturwissenschaftlichen Fakultät
der Universität Bern

vorgelegt von

MARIA IAKOVLEVA

von St.Petersburg

Leiter der Arbeit:
Prof. Dr. Peter Wurz
Physics Institute
Space Research and Planetary Sciences

Von der Philosophisch-naturwissenschaftlichen Fakultät angenommen.

Der Dekan
Bern, DATUM   Prof. Dr. Silvio Decurtins

Abstract

Research of the space environment is a very important and popular subject of present-day science. Different space missions are currently on the way to their subject of investigation (BepiColombo, Mars Express, Rosetta and others). One of the most significant questions to answer, amongst others, is the origin of the Solar System. There are different possibilities to study the space environment: Earth based and the *in situ* researches. The main subject of this work is a *in situ* research technique Time-of-Flight Mass Spectrometry and its application in the space investigation.

The history of our solar system begun about 4.6 billion years ago. The giant molecular cloud collapsed and our Sun was formed. Later, the planets, asteroids, comets and meteoroids were formed from a disc of a pre-planetary matter. There are bodies in the solar system that are so far from the Sun that they probably never have been heated. The matter of such bodies probably includes the unchanged pre-solar grains. Research of such bodies is of great interest. Space mission Phobos-Grunt of Russian Space Agency ROSKOSMOS is a mission to Phobos, one of the two Mars satellites. This mission has two aims: on one hand, surface material of Phobos will be collected and sent back to Earth, on the other hand, there will be several instruments for *in situ* measurements. One of these instruments is a laser ablation time-of-flight mass spectrometer LASMA, that will be specified in this work.

Contents

1 Introduction

1.1 Phobos-Grunt

The question about the origin and evolution of our Solar System is a fundamental one and thus of wide spread scientific interest. To study this question, it is important either to deliver samples of primordial matter for laboratory study to the Earth or to study the primordial matter *in situ*.

On one hand, such material can be quite easily found on Earth in the form of meteorites. The meteorites are a powerful scientific object, that can be used for the study of early Solar System despite such effects as thermal metamorphism, aqueous alteration, brecciation or shock effects, which modified them during entry and descent through the terrestrial atmosphere, and the following residence on the ground (terrestrial weathering process (i.e., chemical and erosional)) and also as part of the parent melt. On the other hand, such matter has been preserved in a primordial condition on some of the small bodies of the planetary system: asteroids, small satellites of planets and comets. On the planets and their larger satellites, which have suffered considerable transformation as a result of magmatic differentiation, erosion and other processes, the search for primordial material is considerably more difficult. Taking into account the extraordinary importance of the determination of the origin and evolution of the planetary system, the project of bringing material from Phobos, one of the satellites of Mars, to the Earth, was chosen by the Russian Space Agency ROSKOSMOS.

1.1.1 Phobos, the moon

Phobos is the largest and innermost of the two moons of Mars. It was named after Phobos, son of Ares (lat. Mars) from Greek mythology. Phobos orbits closer to a major planet than any other moon in the Solar System. Phobos was discovered by the American astronomer Asaph Hall on 18 August 1877. Some important data about Phobos are presented in table below:

Orbital characteristics		
	Mean orbit radius	9378.5 km
	Circumference	58.915 km
	Eccentricity	0.0151
	Periapsis	9235.6 km
	Apoapsis	9518.8 km
	Revolution period	7 h 39.2 min
	Avg. orbital speed	2.138 km/s
Physical characteristics		
	Inclination	1.0756° (to Mars' equator)
	Mean diameter	22.6 km (27×22×19)
	Oblateness	$0.31 - 0.12$
	Surface area	~ 6.100 km^2
	Volume	$\sim (5689 \pm 60)$ km^3
	Mass	$(1.067 \pm 0.003) \cdot 10^{16}$ kg
	Bulk density	(1876 ± 20) kg/m^3
	Surface gravity	$0.0019 - 0.0084$ m/s^2
	Escape velocity	0.011 km/s
	Rotation velocity	11.0 km/h (at the longest axis tips)
	Axial tilt	0°
	Albedo	0.071 ± 0.012
	Surface temp.	≈ 233 K
	Atmospheric pressure	no atmosphere

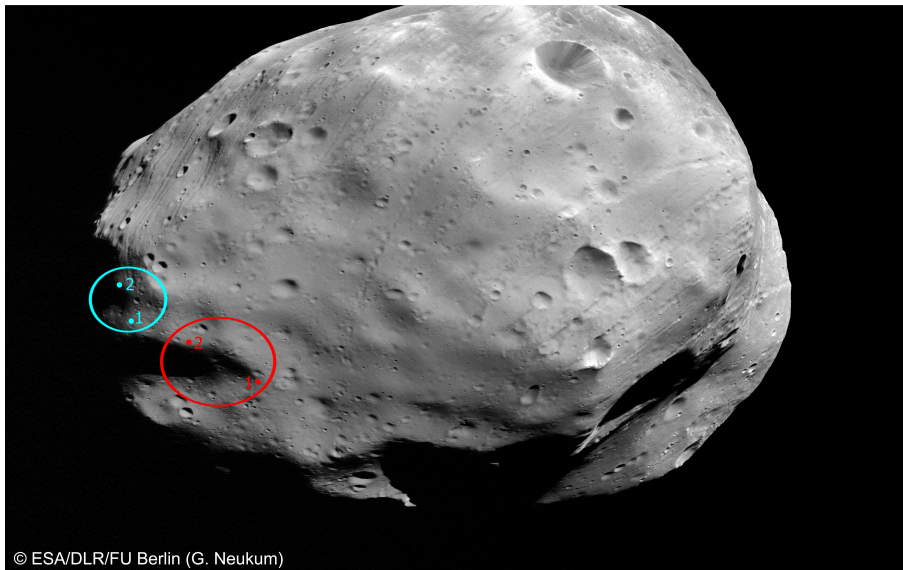Table 1: Characteristics of Phobos and its orbit.

Figure 1: Image of Phobos taken during a Mars Express close flyby of martian moon Phobos. The ellipses marked the previously planned (red) and currently considered (blue) landing sites for the Russian Phobos-Grunt mission [1].

Both, Phobos and Deimos (the second moon of Mars) have very circular orbits which lie almost exactly along the martian equatorial plane. Phobos orbits Mars below the synchronous orbit radius, meaning that it moves around Mars faster than Mars rotates itself. The low orbit of Phobos means that tidal forces are lowering its orbit at the rate of about 1.8 meters per century [2] and it is estimated that in about 40 million years Phobos will either impact the surface of Mars or (more likely) break up into a planetary ring. In contrast, Deimos is slowly moving farther away from Mars. Phobos has an irregular shape (intermediate between a prolate and oblate spheroid). The Soviet spacecraft Phobos 2 detected in 1989 a faint but steady outgassing from Phobos. Images from Mars Global Surveyor and Mars Express indicate that Phobos is covered with a layer of fine dust similar to the regolith on the Earth's Moon and about a meter thick [2]. Because of its ellipsoidal shape, the gravity on Phobos' surface (from one side to another) varies by a factor of about 2.1 (see Table 1). Phobos exhibits differences in surface color: less reddened area in region of Stickney crater and more reddened area anywhere else (Fig. 3 with respect to a solar spectrum).

1.1.2 The origin of Phobos

The origin of Phobos, as well as the origin of Deimos, is still one of the important questions in the planetary science community. The possible way

3

to answer this question is to do *in situ* measurements or to collect samples from the surface of Phobos and to bring them to the Earth for laboratory study. (The Kaidun meteorite (that fell on 3 December 1980) was suggested to be a likely sample of Phobos [3]).

Figure 2: Phobos, the large crater to the left is Stickney (11.3 km in diameter) and the moderately-sized crater within Stickney is Limtoc. North is roughly 30° right of vertical [4].
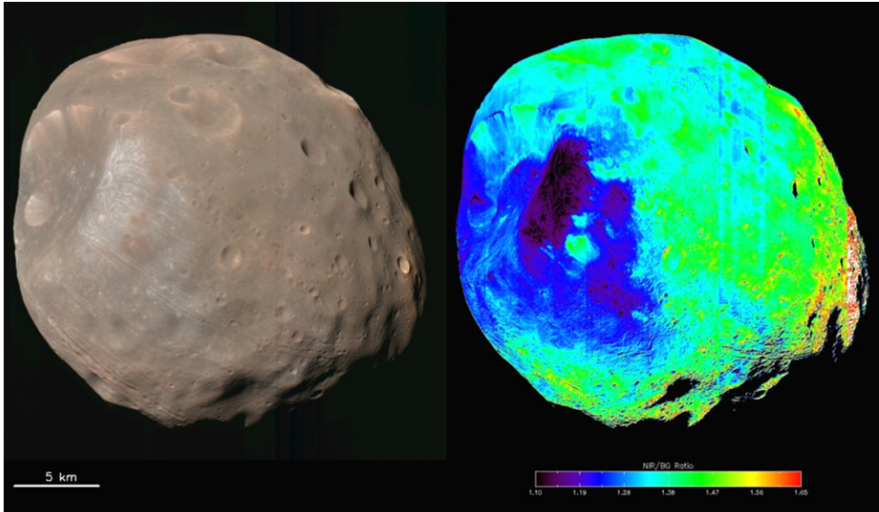
Figure 3: Surface of Phobos. Left: true-color image. Right: false-color representation of the color ratio for a section of image on the left side. Relatively blue regions are shown as blue or black. Yellow and red regions are more strongly reddened with respect to a solar spectrum [4].

To find a plausible creation theory of martian moons, the suggested theory should explain all or at least most of the properties of Phobos (as well as Deimos and Mars) and effects on its surface. Some of them are:

- Form and geological features on Phobos (crater Stickney, grooves), Fig. 1 and Fig. 2

- Extremely circular orbits of both moons (eccentricity of 0.01511 for Phobos and 0.00024 for Deimos)

- The Laplace plane of both moons is very close to the martian equatorial plane (see Tab. 1)

- Low density (see Tab. 1)

- Low geometric albedo (see Tab. 1)

- Comparison of the Thermal Emission Spectrometer (TES, data from Mars Global Surveyor) data to the meteorites shows that no class of chondritic meteorites provide significant agreement with the spectral features observed (Fig. 4 and Fig. 5 [8]).
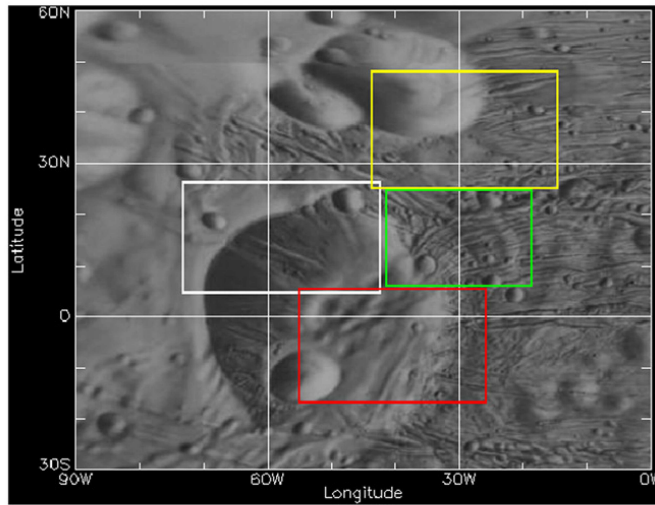
Figure 4: Spatial locations of the spectral clusters derived from TES observations near Stickney Crater on Phobos [8].
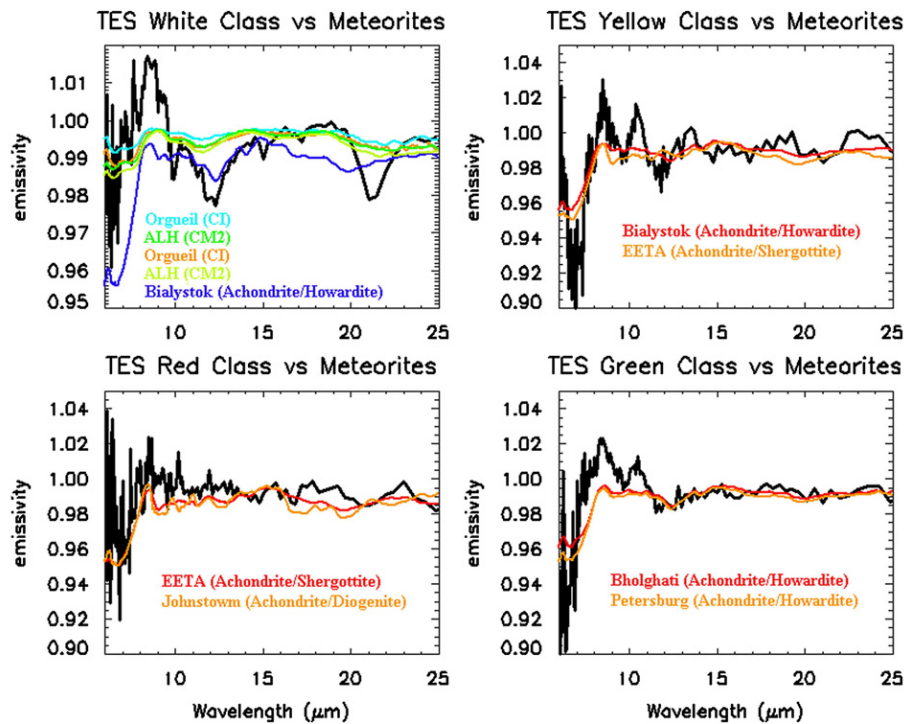

Figure 5: Comparison between TES spectra and meteorites spectra. Only "best" matches are shown. Meteorites spectra provide poor spectral matches to the TES observations [8].

- Little or no absorption due to H_2O at 3 μm (Fig. 6), indicating a nearly anhydrous surface composition
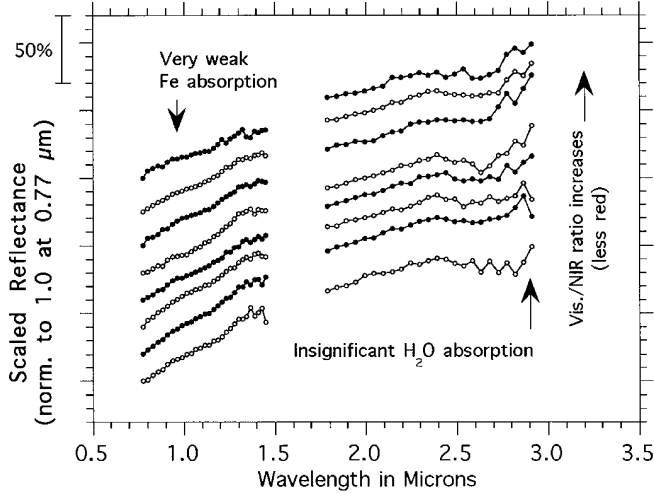

Figure 6: Selection of scaled representative ISM (near-infrared imaging spectrometer) spectra from regions of Phobos having different visible/NIR color ratios as determined by the VSK camera (CCD camera with two channels covering visible and near-infrared wavelengths). Potentially the strongest absorption on the surface of Phobos could be near 3 μm, due to H_2O on hydrate minerals at 2.9−3.1 μm or OH in hydroxylated minerals at 2.7−2.8 μm. Laboratory spectra of a variety of low-albedo meteorite analogs to Phobos show that the H_2O feature exceeds 50% in depth when only $\geq 2\%$ H_2O is present [14]. In the representative ISM spectra of Phobos no 3-μm absorption is consistently resolvable above the level of noise in the data. A conservative upper limit to strength of the absorption is therefore about 10% [9].

- Too high angular momentum of Mars (similar to the Earth-Moon system) [10]

Four different possible scenarios of the origin of the martian moons were proposed by different scientists:

1. Capture of two distinct outer main belt asteroids.

2. Remnant of a larger early moon captured by Mars and later destroyed by its tidal forces.

3. Re-accretion of impact or collision ejecta/debris blasted into Mars' orbit.

4. Co-accretion with Mars from a circum-Mars debris disk.

None of these scenarios can explain all of Phobos's properties at once. Similarity in shape and physical characteristics of surface between small-sized objects of the asteroid belt and Martian moons speaks for the theory of captured bodies. On the other hand, extremely circular and near equatorial orbits of the moons show that there should be some processes after capture that have brought the moons on their current orbits. There should be an explanation of energy loss needed to change the incoming hyperbolic orbit into an elliptical orbit bound to Mars. Tidal orbital evolution could be such explanation, but such orbital evolution scenario implies among others that Phobos and Deimos should have been collied, because collision timescales of 10^5 a [11] are much shorter than the tidal timescales of 10^9 a [12], and that is with high probability not the case. The density of both moons are similar to that of low-albedo carbonaceous C-type asteroids, but their density is lower than most of the samples of carbonaceous material, this requires porosity and/or light elements like water ice in their interiors (Fig. 7). The low bulk density of Phobos provides constraints on its porosity of $(30\pm5)\%$ and hence interpretation of its internal structure. High porosity means, that the body has low structural strength and is not able to survive an aerocapture, and therefore is inconsistent with the capture scenario, that supports *in situ* formation theory. Weak H_2O absorption band at 3 μm differ Phobos from
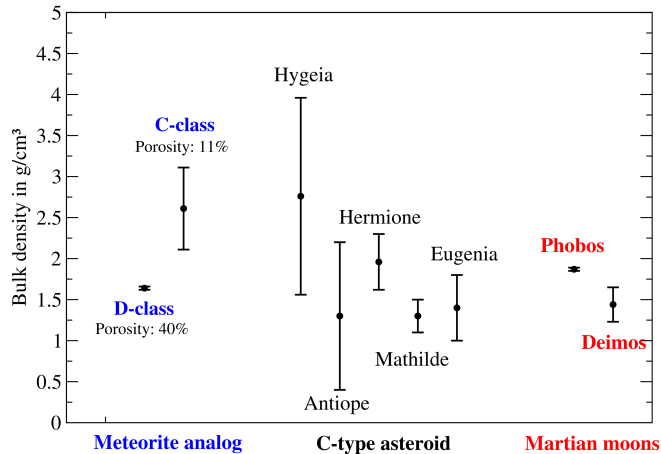
Figure 7: Bulk density of Phobos and Deimos, of low-albedo carbonaceous asteroids and of carbonaceous meteoritic samples [15].

the CI/CM carbonaceous chondrite (like the Murchison meteorite sample) that has been found to fit the slope of the Phobos blue unit spectrum [7] and from the Tagish Lake carbonaceous meteorite (that has been recognized as one possible material analog to D-type asteroids), the albedo of Phobos and Deimos is as dark as the albedo of this meteorite and its spectrum fits

also well the Phobos blue unit. The dehydration could be caused by some dehydration process, such as heating metamorphism, but there is no explanation or source of such process.

The too high angular momentum of Mars could be explained if a planetesimal with 0.02 Mars masses have collided with that planet early in its history [16]. It is also probable that this object impacted Mars at a velocity great enough to vaporize rock (>7 km/s), which is necessary to place large amounts of material into orbit. If material vaporized from the collision with the Mars-spinning planetesimal were placed into orbit, an accretion disk would have resulted. It is possible that as material condensed and dissipated beyond the Roche limit forming small, low-mass satellites due to gravity instabilities within the disk. Once the accretion disk dissipated, tidal forces and libration would have pulled these satellites back down toward the martian surface. In this scenario (Fig. 8), Phobos and Deimos would have been among the first two satellites to form. The low mass of Phobos and Deimos is explained by the possibility that they are composed of loosely aggregated material from the accretion disk, which also implies that they do not contain any volatile elements. Their orbital eccentricity and inclination, which are the most difficult parameters to explain easily with the various capture scenarios, are the natural result of accretion from a circum-planetary disk [10]. This scenario leaves however unexplained several observation too. For example, it requires that the accretion disk could extend beyond the synchronous orbit in order to account for the formation of Deimos.
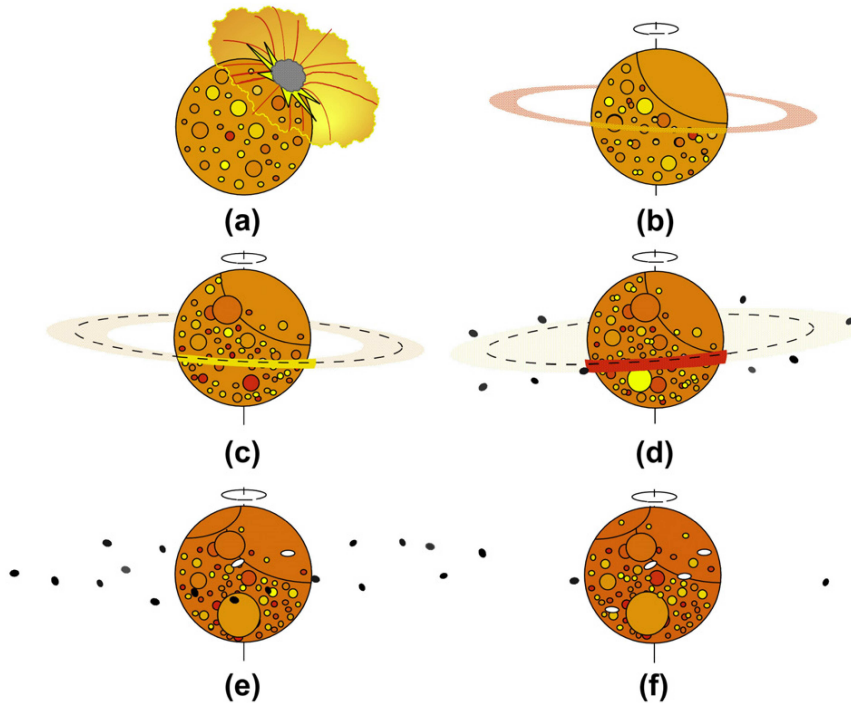
Figure 8: Model for the origin of Phobos and Deimos. (a) Mars-spinning planetesimal collides with Mars vaporizing material and associated large impact basin is formed. Angular momentum imparted to the surface gives Mars its final spin rate. (b) Vaporized material forms an accretionary disk. (c) Materials dissipate past the Roche limit of Mars (dashed line) and begin to coalesce into small moons. (d) Moons continue to form until accretion disk is exhausted. Only Deimos forms outside synchronous rotation. (e) Accretion disk completely dissipates. Dozens of small moons are left orbiting Mars. Tidal perturbations cause these moons to fall back towards the martian surface forming grazing impacts (white ellipses). Development of the Tharsis bulge causes the orbital plane to precess. (f) Present martian system with only Phobos and Deimos in orbit [10].

1.1.3 "Phobos-Grunt" mission: science

The scientific objectives of Phobos research are:

- Study of the origin and evolution of Mars' satellites and their relationship to Mars.

- Determine whether Phobos is an asteroid or body having common origin with Mars, application of results of these researches to the satellite systems of other planets.

- Search for primordial matter of the planetary system and its evolution, determination of geological and radiation ages of matter from Phobos.

- Determination of physical and chemical composition of Phobos

- its inner structure, features and orbital parameters.

- Research of physical terms of near planetary environment close to Phobos (dust and gas components, cosmic rays, magnetic field).

- Interaction of the solar wind with the surface (space weathering).

- Research of possibility of life signature on Phobos.

Scientific payload of the Phobos-Grunt mission includes:

Instrument's name	Manufacturer
• TV system for navigation and guidance	IKI RAS
• Panoramic TV camera	IAS France/IKI RAS
• Stereocamera	IAS France/IKI RAS
• Plasma science package	IKI RAS/Sweden/Ukraine/Germany France
• Micrometeorite detector	Vernadsky Institut of Geochemistry and Analytical Chemistry RAS (VIGAC)
• Ultrastable oscilloscope	IKI RAS
• Sun and stars position detector	IKI RAS
• Scientific data control system	IKI RAS
• Manipulator complex	IKI RAS
• Gas chromotograph	IKI RAS/Germany/France
• Thermal differential analyzer	IKI RAS / Polytechnic University of Hong Kong, China
• Mass spectrometer	VIGAC RAS
• Mössbauer spectrometer	University of Mainz, DE/IKI RAS

Instrument's name	Manufacturer
• Gamma-ray spectrometer	VIGAC RAS
• Neutron spectrometer	IKI RAS/ESTEC
• Laser TOF mass spectrometer	IKI RAS/University of Bern, CH
• Seismometer	IKI RAS / IPE/VIGAC RAS
• Long-wave planetary radar	Insitute of Radio Engineering and Electronic, RAS
• Fourier spectrometer	IKI RAS/Italy/France
• Thermal sensor	VIGAS RAS/Keldysh Institute of Applied Mathematics RAS
• Microscope	IAS France/IKI RAS

Table 2: Scientific payload

There are 3 main ways of studying planets and small bodies of the solar system:

1. Research performed at a distance (remote sensing).

2. Research in laboratory on samples of matter delivered from a planet/small body, i.e. meteorites.

3. *In situ* instrumental measurements made on the surface of bodies from landed spacecraft.

Measuring the surface of Phobos on a landing site of the spacecraft will make it possible to relate information obtained with the contact method in one place (or a few places) to global information from remote sensing. That is important for interpretation of this information. Also it will permit detailed research of regolith properties at the landing place, in particular:

- Elemental and mineralogical composition.

- Inventory of volatile elements.

- Microscopic structure, physical and mechanical properties of regolith.

- Magnetic properties.

One of the *in situ* instruments on Phobos-Grunt is the laser ablation mass spectrometer, LAZMA (a miniature Time-of-Flight Mass Spectrometer) instrument, to investigate the chemical composition of the surface. The Space and Planetary Research Division at the University of Bern participates in the LAZMA instrument at the Co-I level. This contribution is twofold:

1. The majority of the electronics in LAZMA instrument.

2. Co-working on data analysis.

The Space and Planetary Division of the University of Bern has the ability to combine the existing knowledge of laser ablation mass spectrometers with the expertise in the chemical analysis of mineralogical and meteoritic samples.

1.1.4 "Phobos-Grunt" mission: technical data

The automated robotic spacecraft "Phobos-Grunt" (Fig. 9) is intended to return samples of soil from the natural satellite of Mars Phobos to the Earth for laboratory studies. In addition, the Phobos-Grunt mission will investigate Phobos as a celestial body, the regolith at the landing site, plasma-dusty surroundings of Mars will monitor the Mars and celestial-mechanical research. Also a Chinese sub-satellite Yinghuo-1 is scheduled to be released from Phobos-Grunt in a martian orbit with the purpose of carrying out different investigations such as the plasma environment and the magnetic field, or martian ion escape processes and possible mechanisms. Further details are given in the following

Launch	5-8 November 2011
Duration of the mission	3 years
Carrier rocket	"Zenit-2"
Starting mass	13200 kg
Current status of the project	Construction

Plan of the mission

There are several stages in the mission course (Fig. 10):

1. Launch of the spacecraft, its placement into Earth orbit, modification of the orbit for the optimisation of onboard systems.

2. Placing the spacecraft in the departure trajectory and finishing with the approach to Mars at the minimum distance.

3. Orbiting of the sattelite to rendezvous with Phobos.
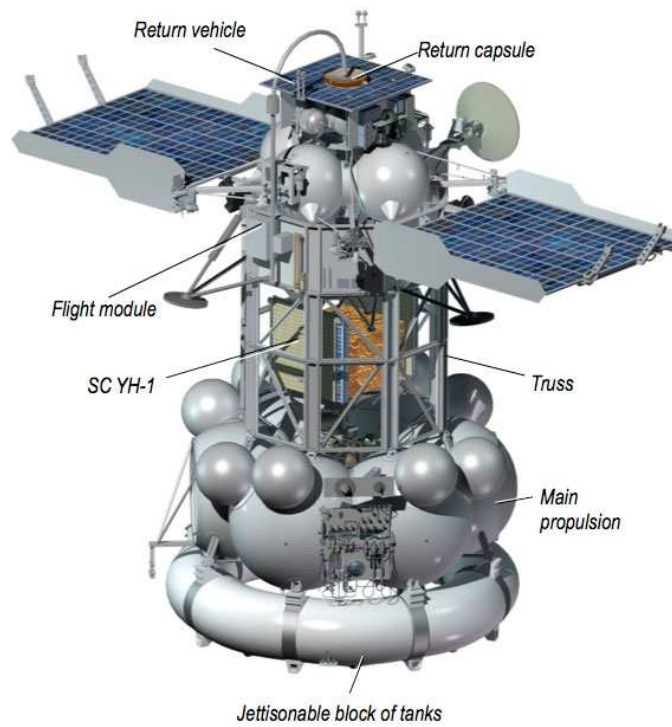
13

Figure 9: Phobos-Grund Spacecraft (development of the Lavochkin Association [37]).

4. Landing in the equatorial region of Phobos.

5. Journey of return capsule back to Earth with soil samples.
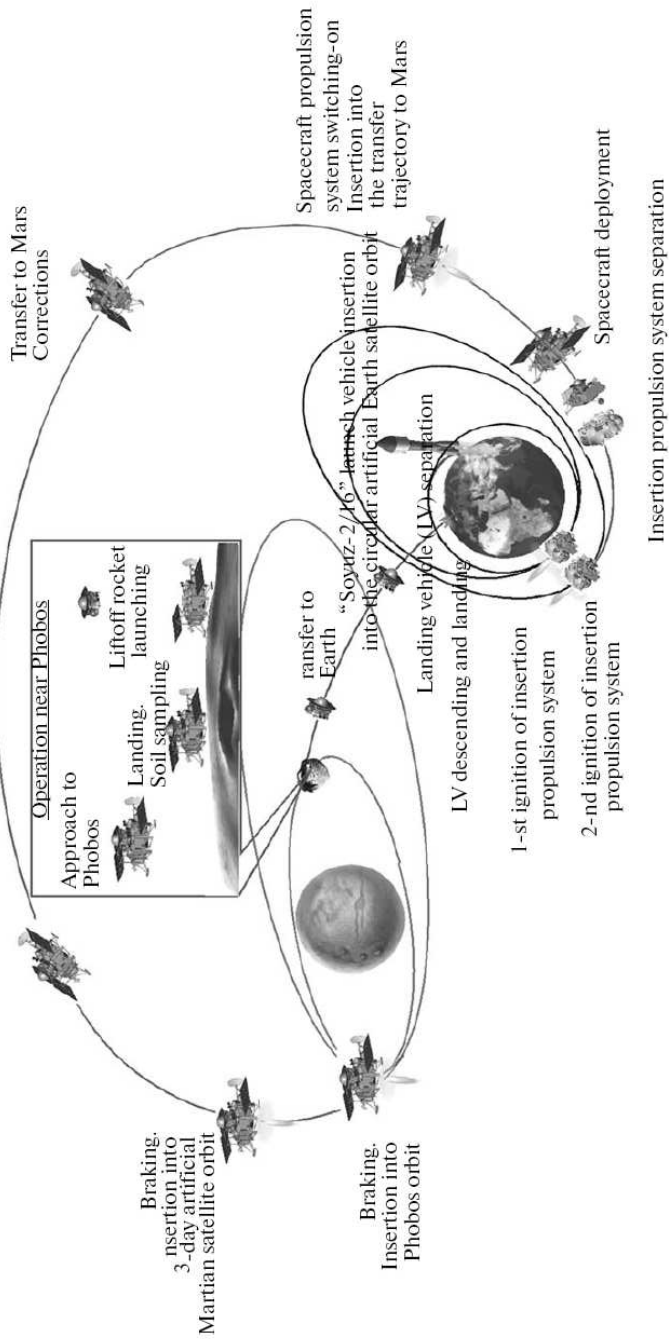
6. Landing on Earth.

Transfer to Mars
Corrections

Spacecraft propulsion
system switching–on
Insertion into
the transfer
trajectory to Mars

Spacecraft deployment

Insertion propulsion system separation

"Soyuz-2/16" launch vehicle insertion
into the circular artificial Earth satellite orbit

Landing vehicle (LV) separation

LV descending and landing

1-st ignition of insertion
propulsion system

2-nd ignition of insertion
propulsion system

Operation near Phobos

Approach to
Phobos

Liftoff rocket
launching

Landing.
Soil sampling

Transfer to
Earth

Braking.
Insertion into
3-day artificial
Martian satellite orbit

Braking.
Insertion into
Phobos orbit

Figure 10: Ballistic scenario of the mission (designed by the Keldysh Institute of Applied Mathematics, RAS, and Lavochkin Association [42]).

1.2 Mass spectrometry

1.2.1 The history of mass spectrometer

Mass spectrometers are analytical instruments that convert molecules into gaseous ions and separate those ions according to the ratio of their mass to charge (m/z). Information from such instruments is generally displayed in a mass spectrum: a plot of relative intensity versus m/z. A mass spectrum can be used to deduce the chemical identity of a compound. For a number of years, mass spectrometers were restricted to the analysis of volatile compounds, or those that could be made volatile by chemical derivatization, and were used primarily for compounds of interest to the natural products or synthetic-organic chemist. In the recent years, ionization techniques have been developed that produce intact molecular ions directly from samples in the liquid or solid phase, thus circumventing the requirement for volatility. Advances in ion optics, ion detection, laser technology, fast recording electronics, signal-processing techniques, and other technologies have been equally important for the development of modern mass spectrometers. This has been particularly true for the time-of-flight (TOF) mass spectrometers, introduced commercially more than 40 years ago [62].

There are other different kinds of mass spectrometers, described by the types of ionization sources, mass analyzers, and (in some cases) detectors that are used. The first mass spectrographs devised by Thomson and Aston used magnetic fields and recorded the resultant spatial dispersion of ions on photographic plates. In 1935, Dempster described an instrument, using a combination of electric (E) and magnetic (B) sectors, that was the forerunner of the double-focusing, high-resolution mass spectrometers in use today (invented by Mattauch and Herzog).

From very early on, mass spectroscopists have been intrigued with the idea that mass spectrometers could be constructed without magnets. In 1946, W. E. Stephens suggested the Time-of-Flight magnetless concept for a mass spectrometer [55].

The Mamyrin Reflectron

In 1973, Mamyrin and co-workers published [23] a design for a high resolution time-of-flight mass spectrometer that included a reflectron for kinetic energy focusing. In this instrument, ions were formed by electron impact and extracted with a dual-stage acceleration system in which the first extraction grid was pulsed [26].
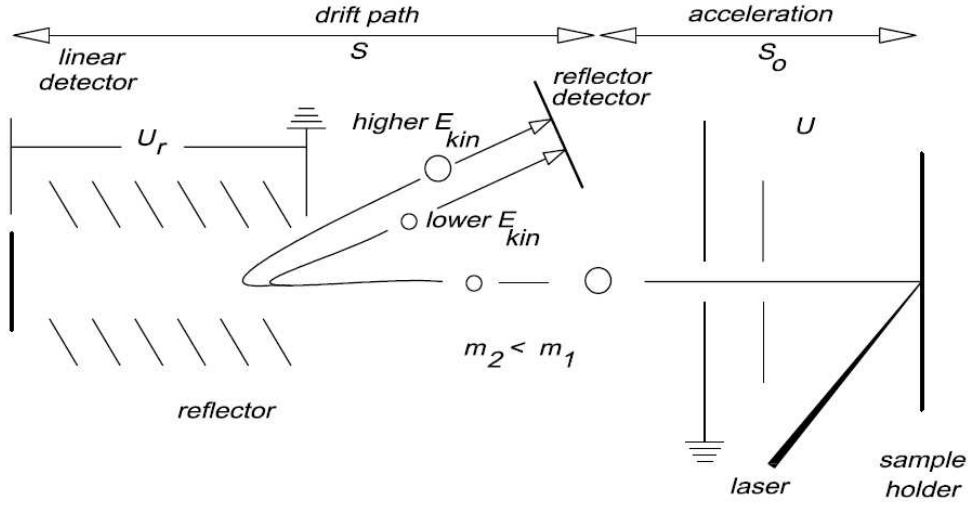
Figure 11: Schematics of reflectron laser time-of-flight mass spectrometer

1.2.2 Basic principle of TOF instruments

The electrical charge q of an ion of mass m_i is equal to an integer number of electron charges e, thus

$$q = ez \tag{1}$$

The energy uptake E_{el} by moving through a voltage U is given by

$$E_{el} = qU = ezU \tag{2}$$

The former potential energy of a charged particle in an electric field is converted into kinetic energy E_{kin}, i.e. into translational motion

$$E_{el} = ezU = \frac{1}{2}m_i{v_i}^2 = E_{kin} \tag{3}$$

Assuming the ion was at rest before, which is correct in first approximation, the velocity attained is obtained by rearranging equation 3 to

$$v_i = \sqrt{\frac{2ezU}{m_i}} \tag{4}$$

i.e., velocity v_i is inversely proportional to the square root of mass.
The idea to measure the time for an ion of unknown m/z to travel a known distance s after having been accelerated by a voltage U is natural. The relationship between the time t needed to travel the distance s is

$$t_i = \frac{s}{v_i} \tag{5}$$

17

when combining equations 3 and 4 one obtains:

$$t_i = \frac{s}{\sqrt{\dfrac{2ezU}{m_i}}} \tag{6}$$

Equation 6 delivers the time needed for the ion to travel the distance s at constant velocity, i.e., in a $field - free$ environment after the process of acceleration has been completed. Rearrangement of equation 6 reveals the relationship between the instrumental parameters s and U, the experimental value of t and the ratio $(m/z)_i$

$$\left(\frac{m}{z}\right)_i = \frac{2eUt_i^2}{s^2} \tag{7}$$

The time necessary to drift through a fixed length of field-free space is proportional to the $\sqrt{(m/z)_i}$

$$t_i = \frac{s}{\sqrt{2eU}}\sqrt{\left(\frac{m}{z}\right)_i} \tag{8}$$

and thus, the time interval $\triangle t$ between the arrival times of ions of different m/z is proportional to

$$\triangle t \sim s\left(\sqrt{\left(\frac{m}{z}\right)_i} - \sqrt{\left(\frac{m}{z}\right)_j}\right). \tag{9}$$

The proportionality of ToF to the $\sqrt{m/z}$ causes $\triangle t$ for a given $\triangle m/z$ to decrease with increasing m/z. Under otherwise the same conditions $\triangle t$ per $1u$ is calculated as 114 ns at m/z 20, 36 ns at m/z 200, and just 11 ns at m/z 2000. Therefore, the realization of a ToF mass analyzer depends on the ability to measure short time intervals with sufficient temporal resolution.

The total ToF is given by

$$t_{tot\ i} = t_i + t_0 \tag{10}$$

where t_0 is an additional time constant caused by the acceleration and the measurement setup. Thus, for $t_{tot\ i}$

$$t_{tot\ i} = \frac{s}{\sqrt{2eU}}\sqrt{\left(\frac{m}{z}\right)_i} + t_0 \tag{11}$$

and for $\sqrt{(m/z)_i}$

$$\sqrt{\left(\frac{m}{z}\right)_i} = \frac{\sqrt{2eU}}{s}(t_{tot\ i} - t_0) = a \cdot t_{tot\ i} + b, \tag{12}$$

where $a = \sqrt{2eU}/s$ and $b = -t_0 \cdot \sqrt{2eU}/s$. This means that $\sqrt{(m/z)_i}$ is directly proportional to the $t_{tot\ i}$ and the constants a and b depend only on the spectrometer. Formula 12 will be used later for mass calibration.

ToF of Multiply Charged Ions   The effect of a charge state $z > 1$ on ToF allows to explain the consequences of higher charge states for isotopic patterns. As z increases to 2, 3 etc., the numerical value of m/z is reduced by a factor of 2, 3 etc., i.e. the ion will be detected at lower m/z than the corresponding singly-charged ion of the same mass. According to equation 8, the ToF is reduced by a factor of $\sqrt{2}$ for doubly-charged ions, which is the same ToF as for a singly-charged ion of half of its mass. Accordingly, the ToF is reduced by a factor of $\sqrt{3}$, for triply-charged ions corresponding to a singly-charged ion of one third of its mass.

In case of multiply-charged ions, the m/z scale is compressed by a factor of z equal to the charge state of the ion. Isotopic distributions remain unaffected as far as the relative intensities are concerned. As the distance between isotopic peaks is reduced to 1/z u, the charge state can readily be assigned.

Reflector ToF Analyzer   In the reflector ToF analyzer (ReToF), the ion-reflector acts as an ion mirror that focuses ions of different kinetic energies in time. Its performance is improved by using two-stage field distribution or even multistage reflector designs. Occasionally, reflector instruments are also equipped with a detector behind the reflector allowing linear mode operation simply by switching off the reflector voltage.

A simple reflector consist of a retarding electric field located behind the fieldfree drift region opposed to the ion source. In practice, a reflector is comprised of rings or less preferably grids at increasing potential. The reflection voltage U_r is set to about 1.05-1.10 times the acceleration voltage U in order to insure that all ions are reflected within the homogeneous portion of the electric field of the device. The ions penetrate the reflectron until they reach zero kinetic energy and are then expelled from the reflector in opposite direction. The kinetic energy of the leaving ions remains unaffected, however their flight paths vary according to their differences in kinetic energy. Ions carrying more kinetic energy will fly deeper into the decelerating field, and thus spend more time within the reflector than less energetic ones. Thereby, the reflector achieves a correction in ToF that substantially improves the resolving power of the ToF analyzer. In addition, the reflector may provide (imperfect) focusing with respect to angular spread of the ions leaving the source and it corrects for their spatial distribution. Adjusting the reflector to have a small angle with respect to the ions exiting from the source allows the reflector detector to be placed adjacent to the ion source (Mamyrin design).

Although the reflector almost doubles the flight path and hence the dispersion in ToF, this effect is of lower importance than its capability to compensate for initial energy spread. Simple elongation of the flight path could also be achieved with longer flight tubes in linear instruments. However,

flight paths that are too long may actually decrease the overall performance of TOF analyzers due to loss of ions by angular spread of the ion beam and scattering of ions after collisions with residual gas.

1.2.3 List of mass spectrometers used in laboratories

To measure the isotopic composition of inorganic samples there are a number of different instruments. The major difference among all these instruments is the process of ion creation. In the following is a list of some of these instruments:

- **TIMS** – Thermal Ionization Mass Spectrometry
  A TIMS is a magnetic sector mass spectrometer that is capable of making very precise measurements of isotope ratios of elements.
  Ionization method: the production of atomic or molecular ions occurs on a hot surface of a metal filament. An ion source with a single-, double-, or triple-filament arrangement is used for the sample evaporation and for the ionization process. Using a single-filament ion source, the evaporation and ionization processes of the substance to be analyzed are carried out on the same filament surface. In the case of a double- or triple-filament ion source, one or two filaments are used for the evaporation of the compound and the gaseous sample molecule (atom) is adsorbed on the surface of the other filament; then, after an electron transfer from the molecule to the filament (production of positive ions) or by the inverse effect (negative ions), the ion can desorb from the filament surface. This process is the same with double- and triple-filament ion sources, but with the triple-filament arrangement a direct comparison of two different samples can be obtained under the same ion source conditions. A double-filament is used instead of a single-filament ion source if it is useful to separate the evaporation from the ionization process. This is valid for the determination of all elements with which the sample compound is evaporated at low temperatures, but a sufficient ion yield is reached only at high filament temperatures. Furthermore, the isotope fractionation effect from evaporation of the sample is higher within the same period of measurement for a single-filament than for a double-filament ion source [31].

- **ICP-MS** – Inductively Coupled Plasma-Mass Spectrometry
  This analyzing method allows the registration of a large number of elements in relatively short time, and as a result of its efficient element detection it is one of the most used procedures for trace element analysis presently.
  Ionization method: The ICP-MS is based on the ionization of the

material in a plasma at about $5000°$C. To produce plasma, a high-frequency current is induced in ionized argon. Out of this plasma the ions are transferred through two apertures (sampler and skimmer) into the vacuum system of the mass spectrometer. After the focusing in the so-called ion optics, the ion beam is separated in ions of different mass in a mass spectrometer [13].

- **SSMS** − Spark Source Mass Spectrometry
  The SSMS method has some unique features that makes it the method of choice for a variety of applications. Almost every material can be readily analyzed. Just a few milligrams of the material are sufficient for analysis (conducting, semiconducting and insulating solids, powders, crystals, liquids, organometallics, ash from organics [18]). The simultaneous detection capability of all elements in a wide concentration range is an important advantage of SSMS over other analytical techniques.
  Ionization method: the formation of ions takes place from a conducting sample brought about by an electrical discharge. The positive ions are accelerated and, after energy selection, separated according to their mass-to-charge ratio in a magnetic field. Detection of the ions can be achieved simultaneously on an ion-sensitive emulsion (photoplate) or sequentially by means of an electron multiplier [33].

- **LAMS** − Laser Ablation Mass Spectrometry
  The LAMS method offers significant potential for the direct analysis of solids. The general principle is: a solid sample of the appropriate size is placed in vacuum chamber and orientated such that its surface is at the focus of the laser beam. The radiation of a solid state laser with an output energy of about $0.1 - 1$ mJ is focused by an optical system on a selected region of the sample and ablates and ionizes some amounts of analytical material which reaches the detector with energy from the laser or by the carrier gas flow.
  Ionization method: when a laser beam of sufficient power density hits a solid surface, material is ejected into the gas phase. In this way, the laser ablates and vaporizes a localized section of solids. The vapor contains significant populations of excited and ionized atoms, which suggests the use of a laser source for elemental analysis by atomic emission spectrometry and mass spectrometry.

In the Bernese laboratory, a LA ToF MS (Laser Ablation Time-of-Flight Mass Spectrometer) is used. The advantages of this system are:

- Small size, suitable for application in space research.

- Small input energy.

- No need of special sample preparation.

- Synchronous release and analysis of almost all elements of the periodical system and their isotopes.

- It allows study of materials with variable physical properties.

2 The LAZMA instrument

A detailed description of the LAZMA instrument is given in [6]. In the following, a short description of the instrument functionality and its technical parameters are given.

2.1 LAZMA instrument

The laser ToF mass reflectron LAZMA is a co-design instrument of Space Research Institute (Russian Academy of Science) and Space Research and Planetary Science department (University of Bern). LAZMA allows investigation and chemical analysis of regolith from the surface of Phobos. The main technical characteristics of the LAZMA instrument are listed below:

Mass range:	1–250 amu
Mass resolution:	380
Relative elemental sensitivity in one spectrum:	10^{-4}
Absolute detection limit by mass in a single analysis:	$5 \cdot 10^{-14}$g
SInstrument speed for 1 amu:	200 ns
Dynamic range:	10^4
Rate of analog-digital transformer (ADT) registration:	15 ns
Elemental abundance accuracy:	10%
Weight:	2.6 kg

The main parts of the instrument are: optical module, analyzer, unit receiving regolith samples and electronic block. The optical module consists of a Nd:YAG laser with a passive Q-switch modulation, focusing optic, an attenuator of laser radiation, and an assembly for the control of laser radiation and synchronization. The analyzer consist of an electrostatic reflector and detector. The unit receiving samples is represented by a disc with 12 cavities (for maximal 11 regolith samples and 1 standard sample for calibration) and applied for the fixation and introduction of the samples to the area of laser radiation and their transportation during the analysis. The electronic block of the instrument provides the power supply of all parts of the instrument, the complete control of the operation of the mass spectrometer, the registration, saving and transmission of the spectral data and telemetry. In Fig. 12, the schematic picture and in Fig. 13, the flight model of the instrument are presented.

2.2 LAZMA science

The instrument LAZMA will provide the isotopic and elemental analysis of the surface regolith layer of atmosphere-free bodies. The laser ablation mass spectrometry research method is well known [34]. A short description of the technique is given in the following:
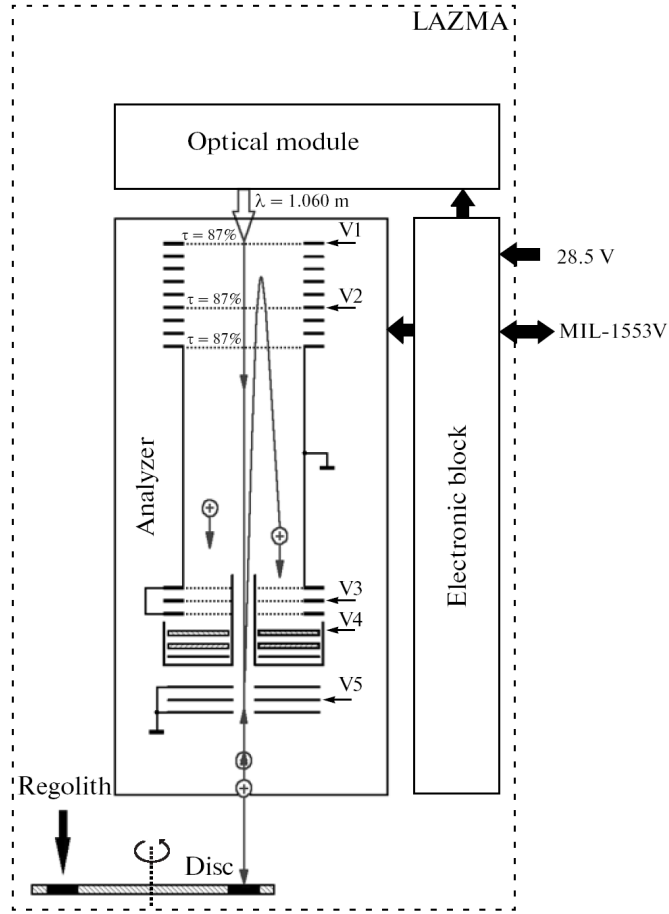
Figure 12: Functional scheme of the LAZMA mass spectrometer [6].

The material destined for the analysis will be loaded by a collecting device onto the sample holder, that position is in the focus of the laser beam. Each laser shot (with duration of 7 ns and power density of about 10^9 W/cm^2) transmits energy to the surface of the sample. As a result of this action, the surface of the sample material will be atomized and ionized and released from the sample in form of the plasma torch. The charged particles emitted from the formed plasma enter the time-of-flight mass analyzer separated by the flight time according to the formula:

$$T = L\sqrt{\frac{M}{2E}} \tag{13}$$

where T is the flight time of ions with kinetic energy E and mass M over the field-free distance L. Ions separated in time, after their reflection in

24
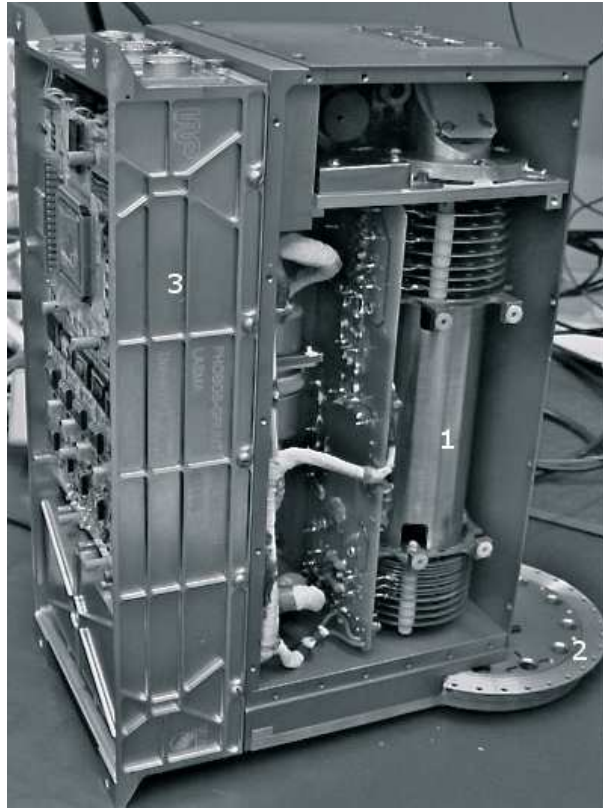
Figure 13: LAZMA instrument, flight model. 1) Analyzer part, 2) rotary disk, 3) electronic block [6].

the deceleration field of the electrostatic reflector, are detected by a micro-channel plate (MCP) assembly. From the exit of the MCP assembly, the signal comes to the high-speed analog-digital transformer and is saved in the instrument's memory as a single spectrum. The time, that an ion needs to reach the detector is determined by its mass (see Eq. 8). Aside from its mass, an element may be recognized according to the distribution and amplitude of the different isotopes, and then the intensity of the mass peaks of the elements may provide the chemical, elemental and isotopic composition of the studied material. The analysis of the spectra allows the determination of the soil type and its mineral composition. Furthermore, LAZMA allows us to study minerals of different physical properties, including finely dispersed powder. The design of the sample holder (rotating disc with 12 different holes) enables the sample analysis to be collected from different positions of the Phobos surface. Also while analyzing the samples the space weathering effects (solar wind, micrometeoritic impacts, cosmic rays) [46] and the influence of the landing apparatus on the surface of Phobos will be investigated.

Four channel registration system of the instrument allows a parallel collection of signals both from elements of the matrix and admixture with a dynamic range of 10^{-5}. Different channel sensitivity allows to reconstruct the spectra for the hole intensity range. In addition, there is a reliability not to lose all data if one of these four channels fails. Ratio between channels referred to electronic specification:

Ch1/Ch2 = 10.08

Ch3/Ch4 = 9.80

Ratio between channels referred to peak comparison:

Ch1/Ch2 = 10.22±0.25

Ch2/Ch3 = 6.54±0.91

Ch3/Ch4 = 9.79±0.33

Although the ratio Ch2/Ch3 can only be estimated trough peak comparison. With help of this data a complete spectrum can be build up (Fig.)

2.3   Instrument's mass scale calibration

While final testing, series of calibration measurements have been done. As a target for the first part of mass scale calibration tests, a tungsten alloy (WC - 68%, TiC - 11.9%, TaC -6.0%, NbC - 4.0%, Co - 9.5%) was chosen. The known relation between mass and time of flight of ions is

$$\sqrt{\left(\frac{m}{z}\right)_i} = a \cdot t_{tot\ i} + b \tag{14}$$

where a and b are the calibration constants. This means for m:

$$\left(\frac{m}{z}\right)_i = (a \cdot t_{tot\ i})^2 + 2 \cdot a \cdot b \cdot t_{tot\ i} + b^2 \tag{15}$$

For a calibration procedure one takes the main isotopes of known elements of the spectrum and calculates the calibration constants a and b (Fig. 14).
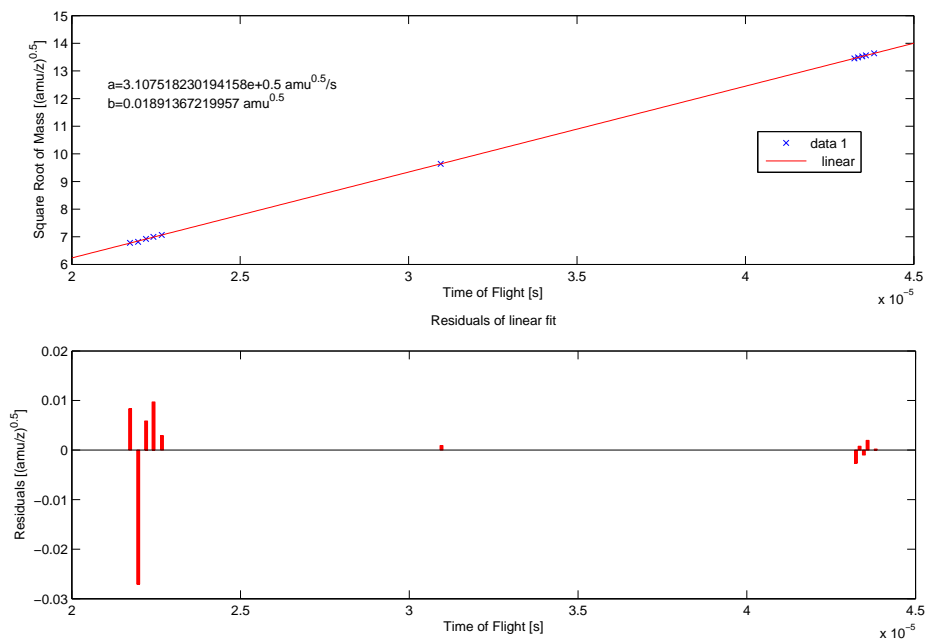
Figure 14: LAZMA mass calibration

After the calibration procedure, all distinguishable isotopes of the spectrum should lie on their mass number $\pm$ 0.5 amu/z or less. After calibration of a LAZMA spectrum, a mass spectrum (e.g. Fig.15) can be produced: Figure 16 shows the detailed resolution for elements Ti, Co, Nb and W.
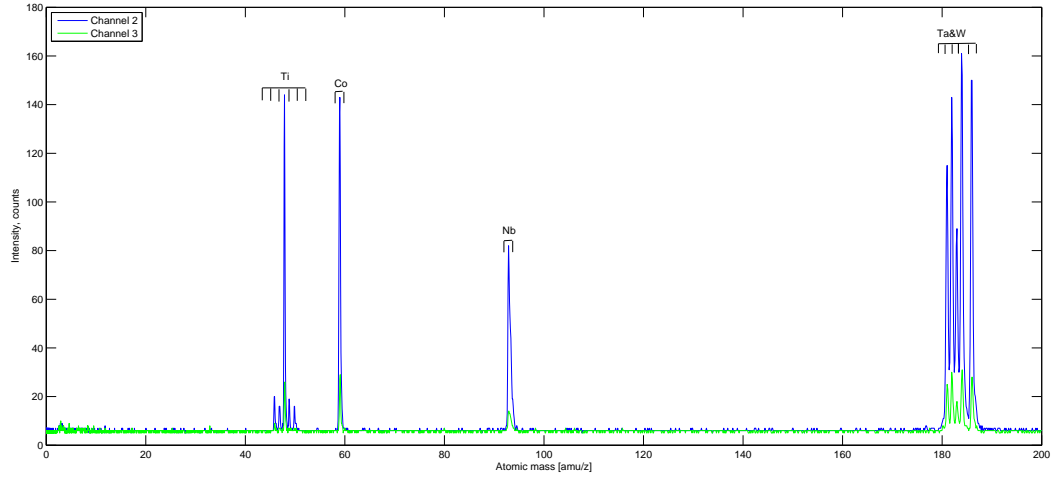
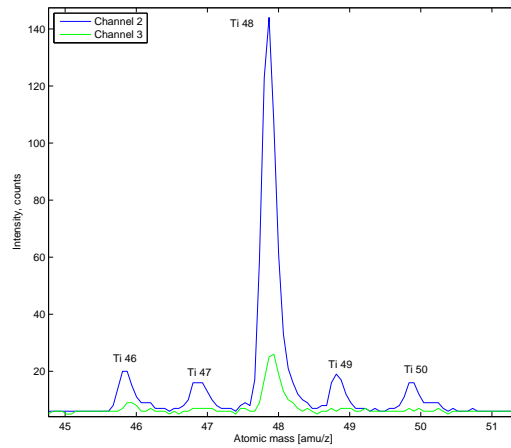Figure 15: LAZMA mass spectrum of the tungsten alloy.

In the second part of the mass calibration, the calibration parameters were tested on a target material JSC-1 [61]. JSC-1 (named after Johnson Space Center) is a lunar regolith simulant. It is a glass-rich basaltic ash which approximates the bulk chemical composition and mineralogy of some of the lunar soils. Major element composition of JSC-1 are listed in Table 3.

| Oxide	Average weight(%)	Std. dev.	% Rel. std. dev.
SiO_2	47.71	0.10	0.21
TiO_2	1.59	0.01	0.63
Al_2O_3	15.02	0.04	0.27
Fe_2O_3	3.44	0.03	0.87
FeO	7.35	0.05	0.68
MgO	9.01	0.09	1.00
CaO	10.42	0.03	0.29
Na_2O	2.70	0.03	1.11
K_2O	0.82	0.02	2.44
MnO	0.18	0.00	-
Cr_2O_3	0.04	0.00	-
P_2O_5	0.66	0.01	1.52

Table 3: Major element composition of JSC-1 [61].

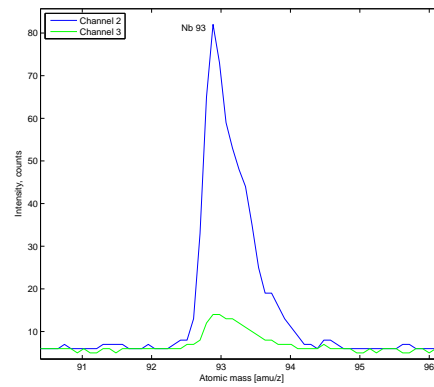The trace element concentrations in JSC-1 are listed in Table 4.

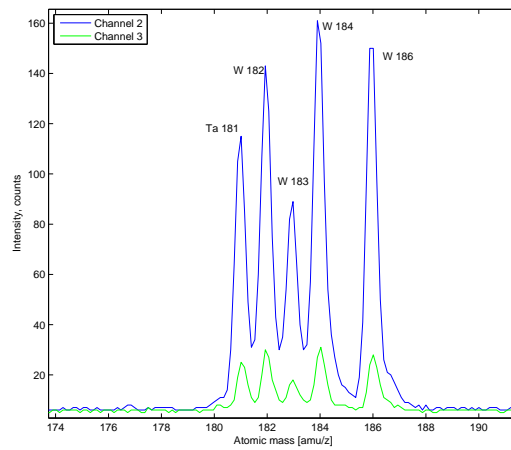With the constants a and b (Eq. 15), which were estimated from the

28

(a) Ti
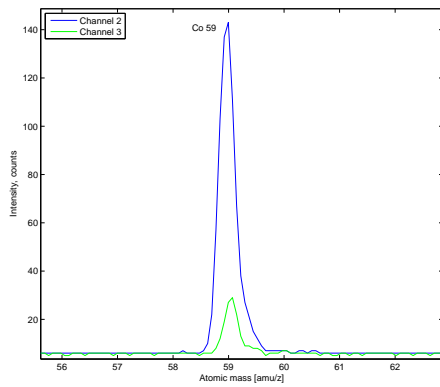
(b) Co

(c) Nb

(d) Ta & W

Figure 16: LAZMA mass spectrum of the tungsten alloy, detailed resolution on (a) Ti, (b) Co, (c) Nb, (d) Ta and W.

Element	Conc. (ppm)	Std. dev.(ppm)
Sr	860	36
Ba	822	13
Ni	137	18
Zr	125	3
Ce	94.6	6
La	48.2	0.9
Co	47.7	1.6
Nd	42	2

Table 4: Trace element concentration in JSC-1 [61].

tungsten alloy calibration, the mass scale of the JSC-1 spectrum can be calibrated, as shown in Fig. 17.
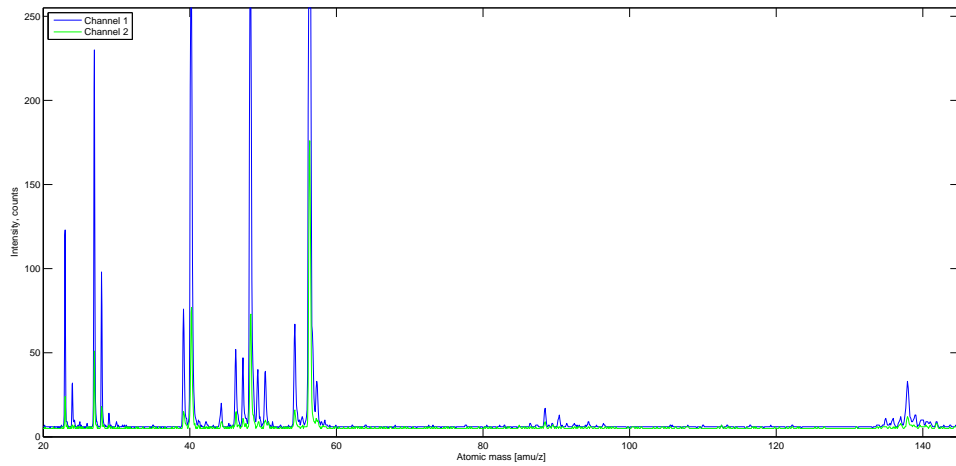

Figure 17: LAZMA mass spectrum of JSC-1.

Details of the mass spectrum of the tungsten alloy are shown in the Fig. 18 and Fig. 19.

The sensitivity of the instrument also allows to see the important trace elements of the spectrum (Fig. 20).
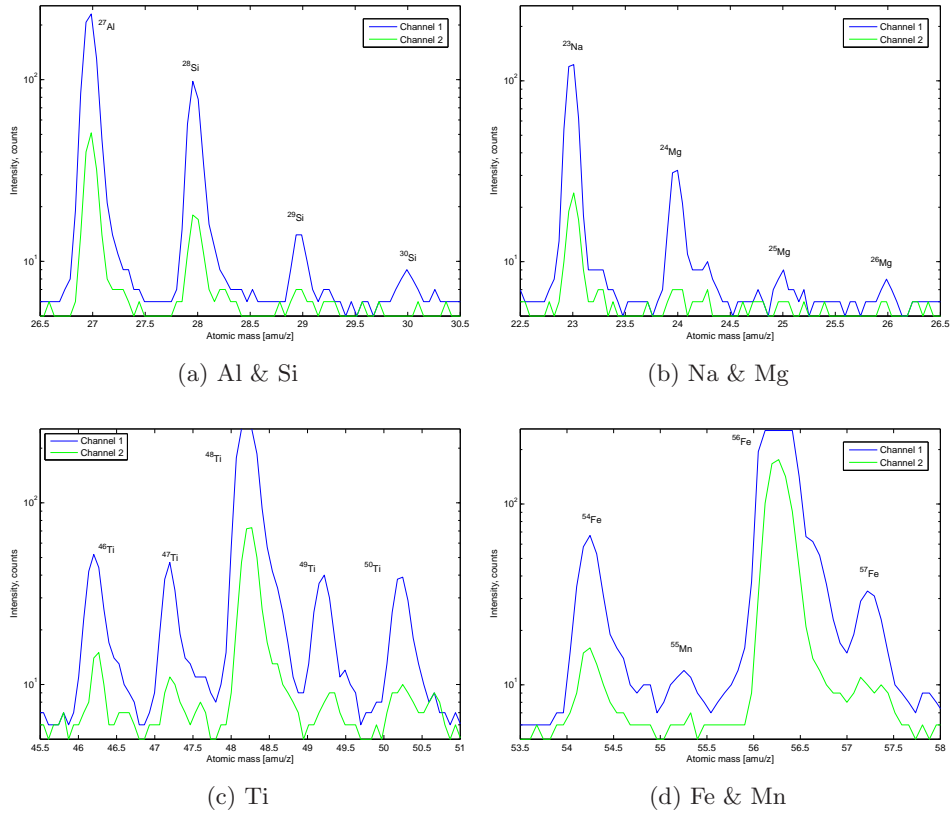
Figure 18: LAZMA mass spectrum of JSC-1, detailed view of (a) Si and Al isotopes, (b) Na and Mg isotopes, (c) Ti isotopes, (d) Fe and Mn isotopes.

The basic (quantitative) abundance calibrations will be made after reception of LAZMA measurements data on Earth. Then it will be possible to simulate the soil similar to that on Phobos. On this simulated soil the quantitative calibration for definition of the statistical characteristics of the received spectra will be made.
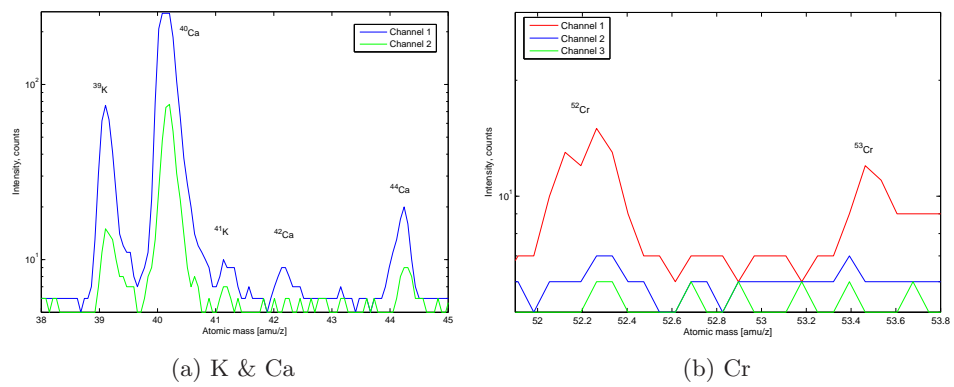
(a) K & Ca

(b) Cr

Figure 19: LAZMA mass spectrum of JSC-1, detailed view of (a) K and Ca isotopes, (b) Cr isotopes.

(a) Sr

(b) Ni & Co

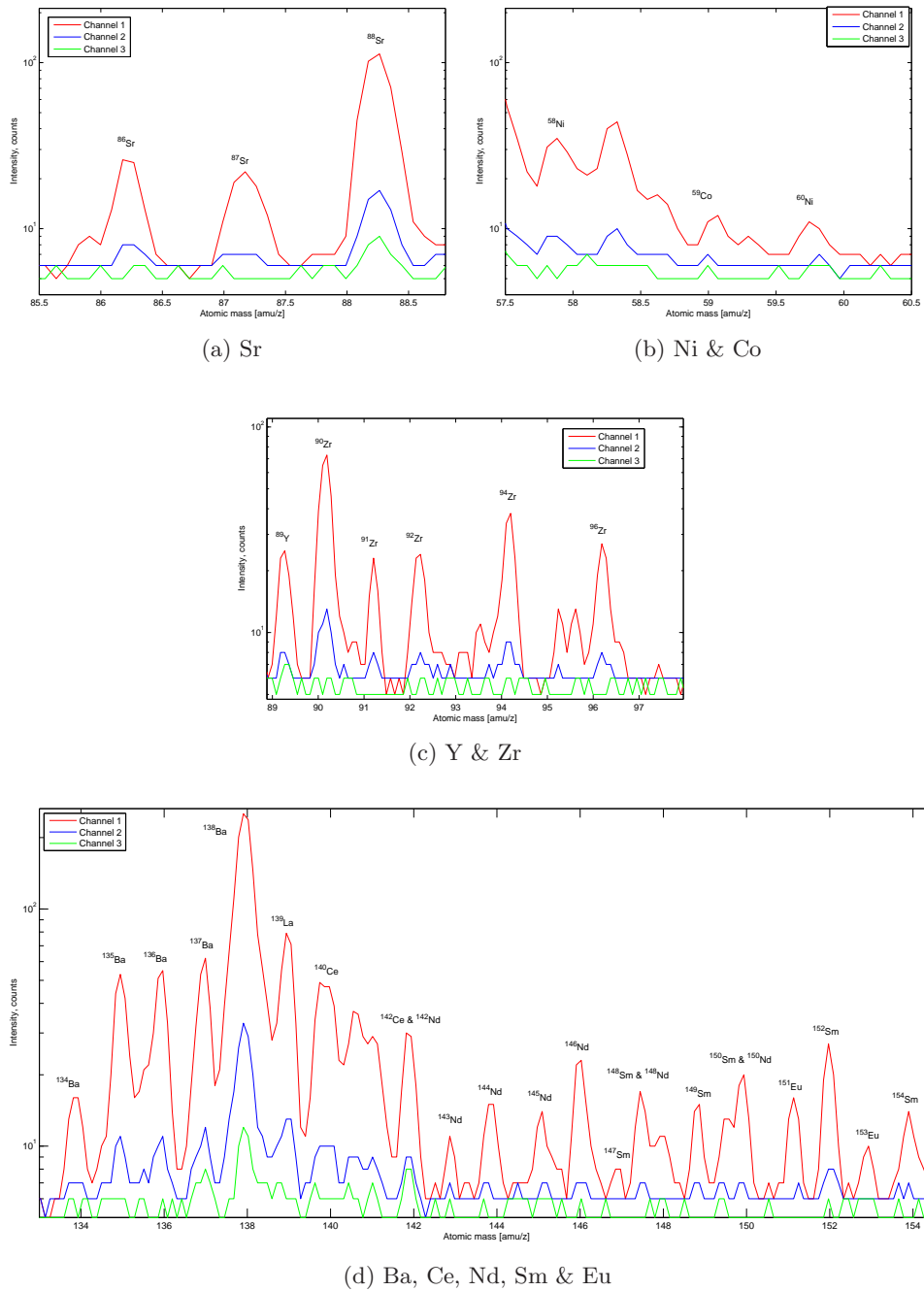(c) Y & Zr

(d) Ba, Ce, Nd, Sm & Eu

Figure 20: LAZMA mass spectrum of JSC-1, detailed view of trace elements (a) Sr, (b) Ni and Co, (c) Y and Zr, (d) Ba, Ce, Nd, Sm and Eu.

3 Laser Ablation Mass Spectrometry (LMS) Laboratory

3.1 Short description

Figure 21 shows a picture of the bernese LMS laboratory setup. This laboratory was originally set up to develop LMS system [54] for the BepiColombo mission [43], where a Mercury lander was a part of the initial mission strategy. Two LMS instruments were developed for an application in on airless planetary surface for this mission. With the Phobos-Grunt mission also supportive studies of LMS spectra from mineral samples are recorded with the existing instrumentation. The laboratory is placed in a clean environment and is supplied with modern technology such high quality optics and modern vacuum chamber.

3.2 Different laser systems

During our work on the project different lasers were used which were possible candidate for a space application (small size, small power requirement). The originally used Nd:YAG microchip laser with 1064 nm and 532 nm [??] were not available anymore. At the beginning of new project (LAZMA) it was decided to use Kigre laser system with 1.54-μm wavelength because of its small dimensions and high peak power. During the work with this laser the instability of the laser beam intensity was recognized. That was a big constraint for the mass resolution of the spectra. Due to this problem it was determined to use a regular laboratory laser with more stable output energy, Brio laser, for the measurements supporting the LAZMA instrument. The Brio laser is not a flight spare, but it allows the study of the influence of different wavelengths on a mass spectra.
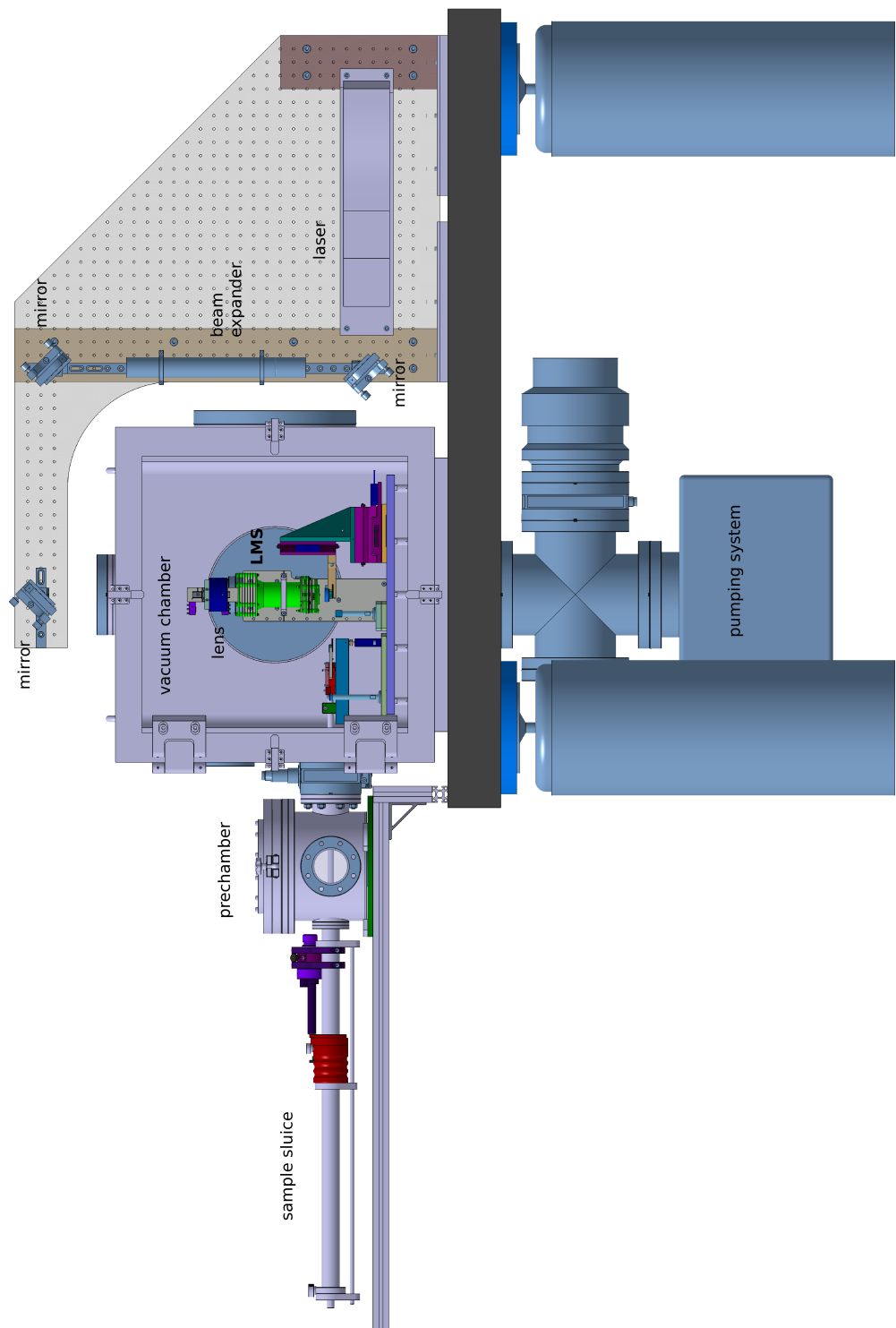
Figure 21: Bernese LMS labor equipment.

3.2.1 Kigre (1534 nm)

In our setup lab-prototype we use the MK-88 10 Hz laser from KIGRE, Inc. The laser performance data is shown in the following table

Name	Performance
Laser Wavelength	1.54 μm
Pump Voltage & Amps	8 V, 60 A
MK-88-1 Output Energy & Mode	$\sim$ 3 to 4 mJ TEM$_{00}$
Laser Output Pulswidth	$\sim$ 7 ns
MK-88-1 Raw Beam Diameter	0.8 mm
MK-88-1 Beam Divergence	$\sim$ 3.5 mrad
Pulse Rep-rate	10 Hz
Pulse-to-pulse Timing Jitter	$<$ 1us
Laser Head Size	0.85`` $\times$ 2.0`` $\times$ 3.0``
Conductive Cooling Requirements	$\sim$ 15 W
Operating Temperature Range	-40 to $+50$ ℃

Table 5: Kigre MK-88 10 Hz laser specifications

This is a compact high efficiency diode pumped erbium glass laser that produce 3 to 5 mJ Q-swiched pulses 1.54 um at 10 Hz. The positive properties such as eye safety or small size were compared with negative properties such as power supply problems or bad warranty supporting. So it was decided to not use this laser in further studies.

3.2.2 Brio (1064 nm, 532 nm, 355 nm, 266 nm)

Name	Performance
Laser Wavelength	1064 nm, 532 nm, 355 nm, 266 nm
Flashlamp Discharge Voltage	690 V
Brio F01 Output Energy at 1064 nm	110 mJ

Continuation on the next page...

Name	Performance
Brio F01 Output Energy at 266 nm	12 mJ
Laser Output Pulswidth	$\sim$ 4 ns at 1064 nm and $\sim$ 3 ns at 266 nm
Brio F01 Beam Diameter	4.5 mm
Brio F01 Beam Divergence	$\sim$ 0.6 μrad
Pulse Rep-rate	20 Hz
Pulse-to-pulse Timing Jitter	< 1 ns
Laser Head Size	73 cm$\times$232 cm$\times$80 cm

Table 6: Brio F01 20 Hz laser specifications

This laser is lamp-pumped pulsed Nd:YAG laser with either fundamental wavelength of 1064 nm, second harmonic at 532 nm, third harmonic at 355 nm or fourth harmonic at 266 nm. Brio F01 laser possesses a physical shatter on laser beam entrance to control the output energy of the beam.

3.3   Detector system

3.3.1   Microchannel plate (MCP) preparation (hole drilling, cleaning, tests)

A microchannel plate (MCP) is an electron multiplier for detecting X-rays, ultraviolet radiation and charged particles. The output is a two-dimensional electron image which preserves the spatial resolution of the original input radiation, but with a linear gain up to 1000. This may be used for exciting a phosphor screen placed close to the output, giving a visual representation of the radiation pattern. Alternatively, the electron image can be for example read out by a wedge-and-strip or fast delay-line anode array [58].

There are 2 different sorts of MCPs in use for our lab setup, both from the same manufacturer PHOTONIS. They are:

- MCP 40/10/8/8 D 46:1 MP 6.4CH EDR MS

- MCP 40/32/25/8 D 40:1 NR EDR MS

The specificity of the second MCP sort is hole absence. The lifetime of one MCP is about 6-8 months. For costs optimizing it was proposed to use the hole-free MCP and to drill a hole by our own.
The procedure of hole drilling is following:
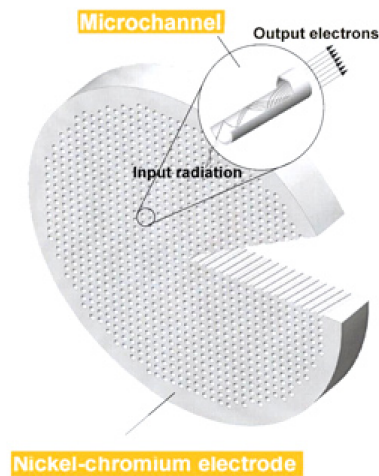
1. put MCP on a holder Nr. 2, Fig. 23

Figure 22: MCP buildup. Each plate consists of an array of tiny glass tubes fused together to form a thin disc. Both faces of the disc are metal-coated to provide parallel electrical connections to all channels. In a vacuum, and with a potential difference (usually 800 to 1400 V) across the plate, each channel becomes a continuous dynode electron multiplier, operating on the same principle (electron avalanche) as its cousin - the single-channel electron multiplier [58].

MCP parameters	MCP 1	MCP 2
Quality Diameter (mm)	40	40
Pitch C-To-C (microns)	10	32
Pore Size (microns)	8	25
Bias Angle (°)	8	8
MCP Grade	Detection	Detection
Aspect Ratio[1]	46:1	40:1
Geometry	6.4 CH[2]	Rimless (NR)
Bias Current	EDR[3]	EDR
Additional Coatings	None	None
Flatness	Standard	Standard
Multiples (Quantity MCPs)	Matched Set (MS)	MS

Table 7: MCP description; ([1]) channel length-to-diameter ratio (L/D); ([2]) 6.4 mm inner diameter Center Hole; ([3]) Extended Dynamic Range.

2. choose a cover plate (one of plates Nr. 3, Fig 23) depending on the channel length (Channel Length=Pore Size×Aspect Ratio)

3. put this setup as it shown on Fig. 24

4. use first the thicker diamond drill (part Nr. 1 left side, Fig. 23) and then fine diamond drill (part Nr. 1 right side, Fig. 23)
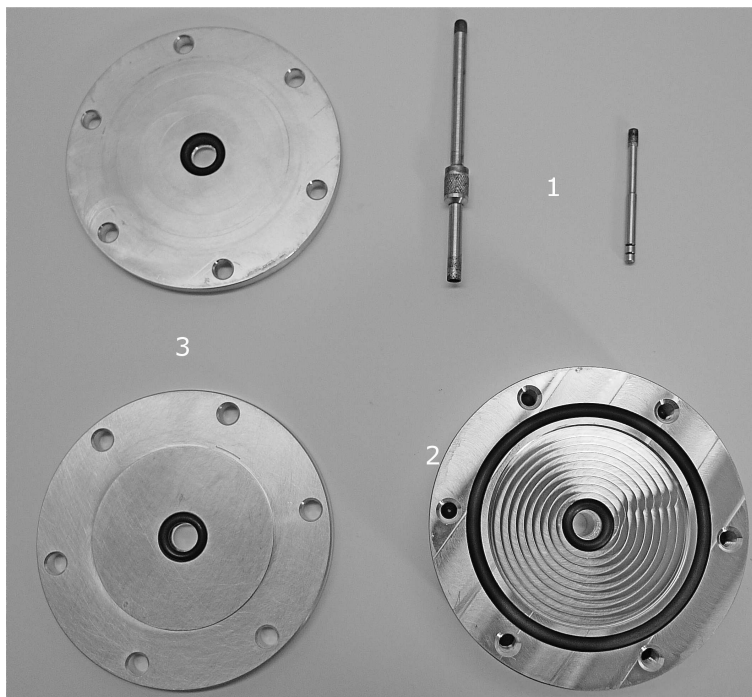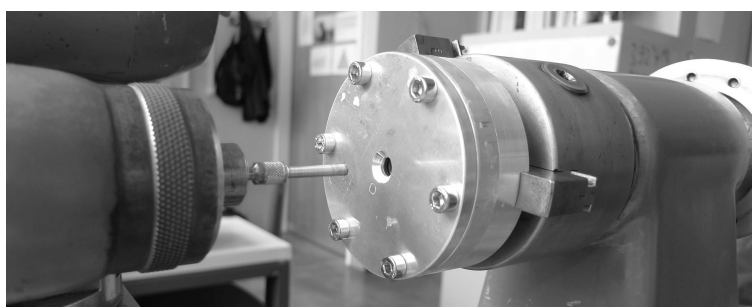

Figure 23: MCP drilling equipment.



Figure 24: MCP drilling machine.

After hole drilling the MCP should be cleaned. To realize the cleaning procedure one needs:

- A primary vacuum chamber, that can be heated up to 60°C (min pressure lower than 0.1 torr). A window is needed to see inside the chamber.

- 2 crystallizing dishes

- watch glasses to dry the MCP (size larger than the MCP)

- Isopropyl alcohol, chemical quality

- ultra pure deionized water

Cleaning procedure

1. put water in a crystallizing dish and make it boiling

2. put isopropyl alcohol in the second dish

3. put the MCP in the dish filled with isopropyl alcohol

4. put the MCP in the dish with isopropyl alcohol in the primary vacuum chamber and pump down till the alcohol is boiling inside the channels of the MCP. This appears suddenly at some millibars. Continue to pump down for 3 or 4 seconds and broke vacuum

5. Remove the dish from the vacuum chamber

6. Remove the MCP from alcohol and put it immediately in the boiling water, push it down in the water with tefzel or teflon pincette, and let them in water during about one minute

7. Remove the MCP from boiling water and put it on the glass watch

8. Dry the MCP on the glass watch during 4 hours at 60°C in primary vacuum

9. Mount the MCP immediately after process and store them in primary vacuum or under dry nitrogen.

On the Fig. 25 a hole edges of MCPs with a hole drilled in workshop in the house are presented. On the Fig. 26 a hole edge drilled by manufacturer is presented for comparison. As one can see there are no significant differences between self made hole and hole made by manufacturer. Thus there are no objections for preparing of MCP in the house.
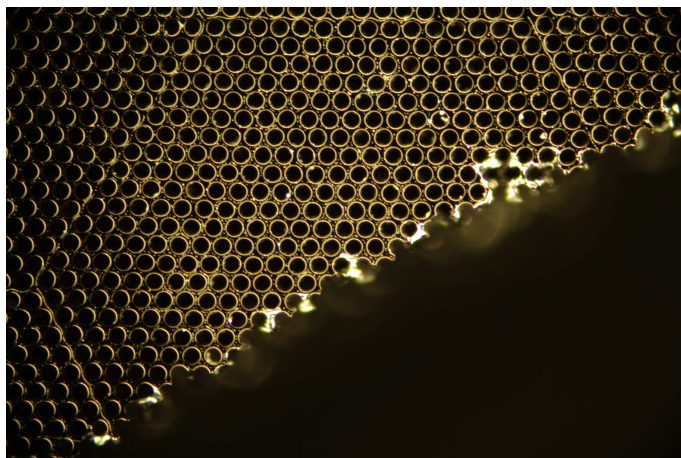
(a) MCP A
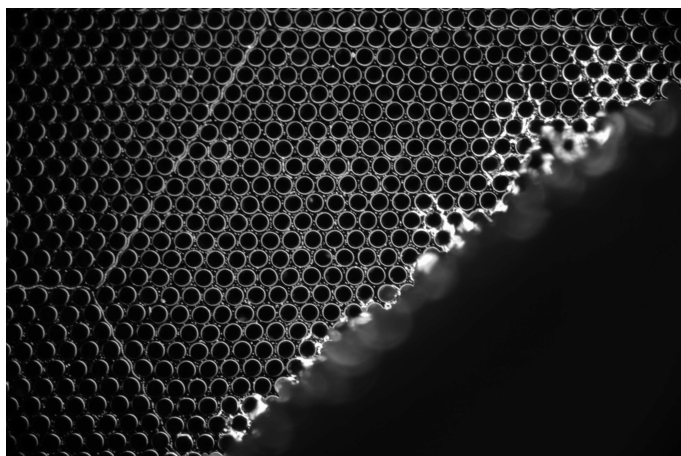
(b) MCP B

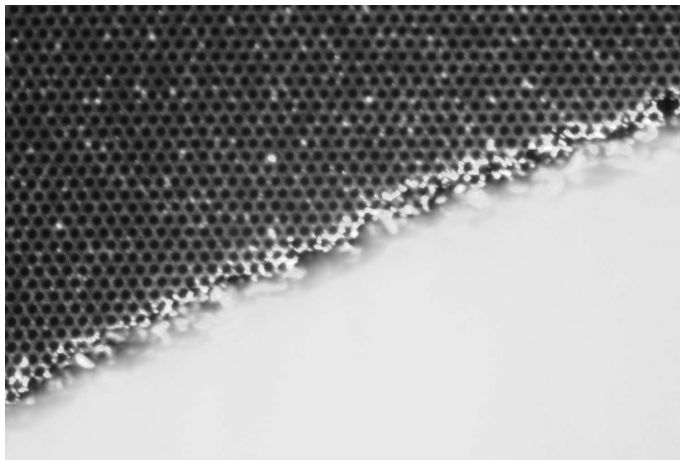Figure 25: MCP with a central hole drilled in house.

Figure 26: MCP with central hole drilled by manufacturer.

MCP Test Resistance measurements were done to test the MCPs before hole drilling, after hole drilling and after 8 months of using of the MCPs. For testing a resistance bridge (Fig. 27) and MCP-measurement setup (Fig. 28) was used.
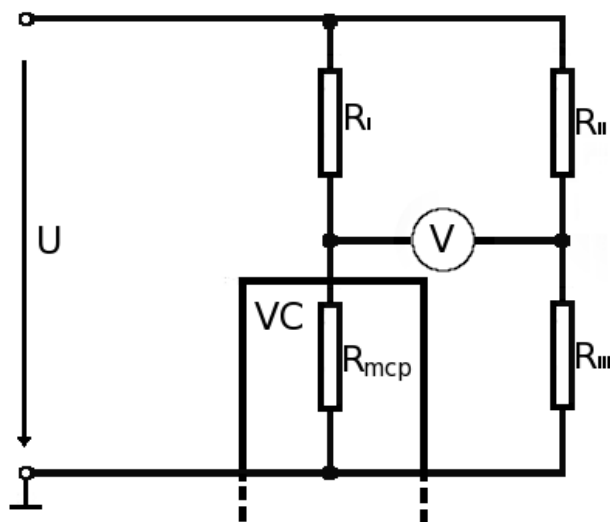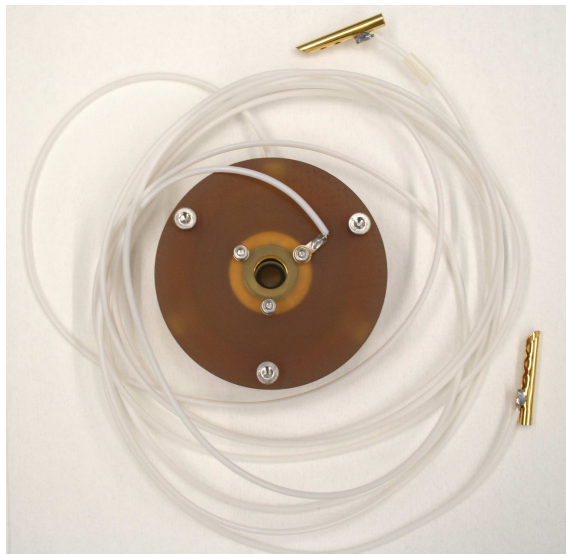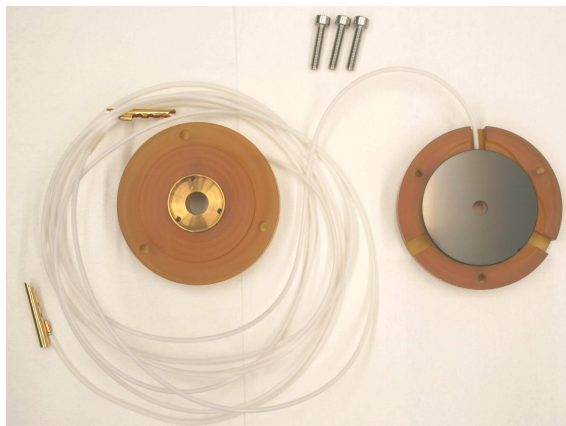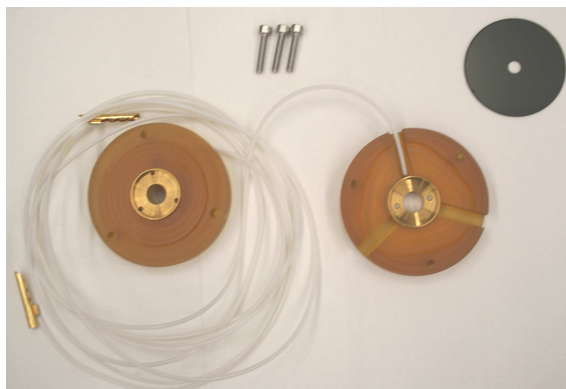

Figure 27: Circuit diagram of resistance bridge. VC - vacuum chamber; R_1, R_2, R_3 are known resistances; R_{mcp} - resistance of micro channel plate, to be defined.
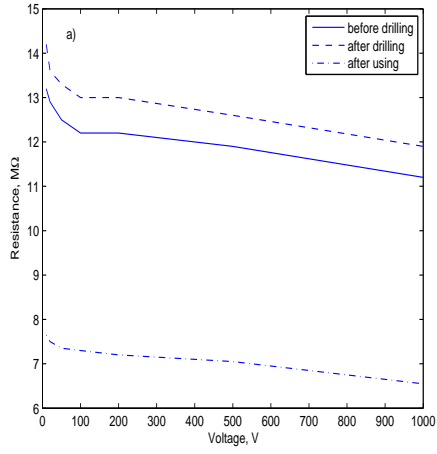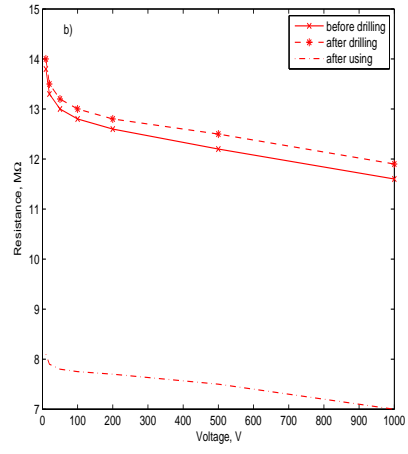
Figure 28: MCP measurement setupf a) closed, b) opened, c) opened, MCP removed.

(a) MCP A   (b) MCP B

Figure 29: MCP resistance evaluation of a) high voltage MCP, b) low voltage MCP.

3.4 LMS labor detector
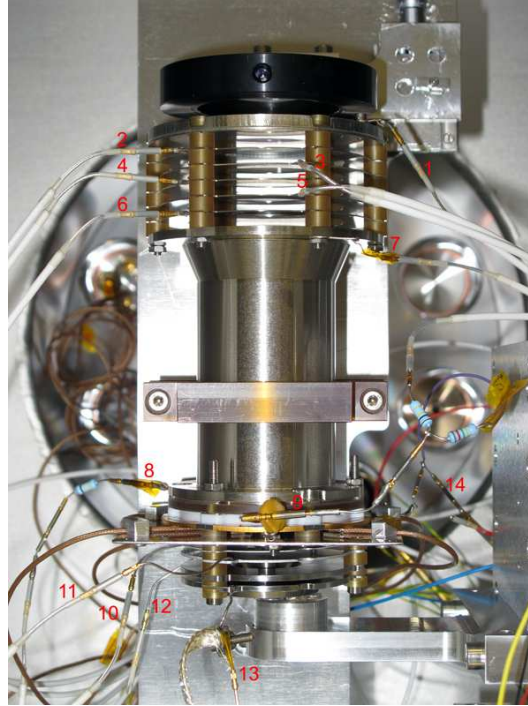
Figure 30: Labor LMS detector.

The explanation for the Fig. 30 :

	Function		Function
1	Backplane	8	Upper MCP's
2	5th ring of reflectron	9	Lower MCP's
3	4th ring of reflectron	10	Lens
4	3th ring of reflectron	11	Snorkel
5	2th ring of reflectron	12	Acceleration
6	1th ring of reflectron	13	Entrance (GND)
7	Drift tube	14	GND MCP's

Table 8

LMS principle of operation : the ions removed by the laser from the target material are accelerated into the mass spectrometer through a small hole and focussed through a narrow tunnel in the centre of the detector toward the reflectron. The ions pass the ToF tube and are reflected by the ion mirror back onto the MCP detector.

4 Galena: Pb-isotope Ratios

4.1 Theoretical fundamentals

4.1.1 The general principles of the isotope geology of lead

The method of the age determination of minerals based on the isotope ratio of lead is described by different researchers, such as Holmes (1946, 1947 and 1949), Houtermans (1946 and 1947), Stacey and Kramers (1975) and others is used in this work. Geochronology makes use of the constancy of the rate of natural radioactive decay. Since a radioactive nuclide decays to its daughter nuclide at a specific rate, one can determine the time of the rock crystallization and other thermal events by determining the ratio of the parent and the daughter nuclide.

The basic equation

The basic equation of radioactive decay is:

$$\frac{dN}{dt} = -\lambda N \tag{16}$$

where λ is the decay constant, N is the number of the radioactive parent nuclide, and dN/dt is the rate of change of the number of parent atoms in time. λ is defined as the probability that a given atom decays in a certain time dt and its unit is in inverse of time. After dividing the left part of equation 16 by N and integration one gets

$$\int_{N_0}^{N} \frac{dN}{N} = -\int_{0}^{t} \lambda dt \tag{17}$$

where N_0 is the number of atoms of the radioactive (or parent) isotope present at time $t = 0$. After integration, the equation 17 is

$$\ln \frac{N(t)}{N_0} = -\lambda t \tag{18}$$

This can be expressed as

$$\frac{N(t)}{N_0} = e^{-\lambda t} \qquad \text{or} \qquad N(t) = N_0 e^{-\lambda t} \tag{19}$$

This is under the assumption that there are no daughter nuclides at the beginning of the decay process and each parent nuclide can decay to exact one daughter nuclide, the number of daughters produced by radioactive decay D^* is the difference between the initial number of parent isotopes and the number remaining after the time t:

$$D^* = N_0 - N \tag{20}$$

Substitution of equation 19 into equation 20 leades to

$$D^* = Ne^{\lambda t} - N = N \cdot (e^{\lambda t} - 1) \tag{21}$$

Thus, the number of daughter atoms produced due to radioactive decay is a function of the number of parent atoms present and time t. Since there will be in general some atoms of the daughter nuclide in the sample source to begin of the process, i.e., when $t = 0$, a more general expression is:

$$D_t = D_0 + N \cdot (e^{\lambda t} - 1) \tag{22}$$

where D_t is the total number of daughter nuclides measured (or in the system) and D_0 is the number of daughters originally present.

^{206}Pb $-^{207}$Pb dating method

The U-Th-Pb system is somewhat of a special case as there are 3 decay schemes producing isotopes of Pb, ^{235}U decays to ^{207}Pb with a half-life $T_{1/2}$=0.704·10^9 years (Tab. 11), ^{238}U decays to ^{206}Pb with a half-life $T_{1/2}$=4.47·10^9 years (Tab. 10) and ^{232}Th decays to ^{208}Pb with a half-life of 14.01·10^9 years (Tab. 9). Since the two parents ^{235}U and ^{238}U are chemically identical and two daughters ^{206}Pb and ^{207}Pb are chemically identical as well, therefore respond in the same way to physical and chemical disturbances, combining the two provides a particularly powerful tool for age determination of a geological system.

									Ra 228 MsTh₁ 5.7 a β⁻	α	Th 232 Th 1.4·10¹⁰a		
										Ac 228 MsTh₂ 6.13 h β⁻			
		Pb 212 ThB 10.6 h β⁻	α	Po 216 ThA 0.15 s	α	Rn 220 Tn 55.6 s	α	Ra 224 ThX 3.64 d	α	Th 228 RdTh 1.9 a			
Tl 208 ThC'' 3.1 m β⁻	α 36.2%	Bi 212 ThC 60.6 m β⁻ 63.8%											
	Pb 208 ThD stable	α	Po 212 ThC' 0.3 μs										

Table 9: Natural radioactive family of ^{232}Th [51].

Some advantages of the ^{206}Pb- ^{207}Pb dating method are:

- In general, ages based on the radiogenic ^{207}Pb/^{206}Pb ratio come closest to the time of crystallization of minerals because such ages are not affected by recent losses of Pb or U.

Table 10 — URAN-RADIUM A=4 n+2

A	Hg	Tl	Pb	Bi	Po	At	Rn	Ra	Th	Pa	U
238											U 238, U_1, $4.5\cdot10^9$ a, α
234									Th 234, UX_1, 24.1 d, β⁻	Pa 234, UX_2, 1.2 m, β⁻	U 234, U_{II}, $2.5\cdot10^5$ a, α
230									Th 230, Io, $8\cdot10^4$ a, α		
226								Ra 226, Ra, 1600 a, α			
222							Rn 222, Rn, 3.8 d, α				
218					Po 218, RaA, 3.05 m, α 99.98% / β⁻ 0.02%	At 218, ~2 s, α					
214			Pb 214, RaB, 26.8 m, β⁻	Bi 214, RaC, 19.8 m, β⁻ 99.96% / α 0.04%	Po 214, RaC′, 162 µs, α						
210		Tl 210, RaC″, 1.3 m, β⁻	Pb 210, RaD, 22 a, β⁻ ~100% / α $0.75\cdot10^{-6}$%	Bi 210, RaE, 5.0 d, β⁻ ~100% / α $5\cdot10^{-5}$%	Po 210, RaF, 138.4 d, α						
206	Hg 206, 8.1 m, β⁻	Tl 206, RaE″, 4.3 m, β⁻	Pb 206, RaG, stable								

Table 10: Natural radioactive familiy of ^{238}U [51].

Table 11 — ACTINIUM A=4 n+3

A	Tl	Pb	Bi	Po	At	Rn	Fr	Ra	Ac	Th	Pa	U
235												U 235, AcU, $7\cdot10^8$ a, α
231										Th 231, UY, 25.6 d, β⁻	Pa 231, Pa, $3.3\cdot10^4$ a, α	
227									Ac 227, Ac, 22 a, β⁻ 98.8% / α 1.2%	Th 227, RdAc, 18.7 d, α		
223							Fr 223, AcK, 22 m, β⁻ ~100% / α $4\cdot10^{-3}$%	Ra 223, AcX, 11.4 d, α				
219					At 219, 0.9 m, α 97% / β⁻ 3%	Rn 219, An, 3.9 s, α						
215			Bi 215, 7.4 m, β⁻	Po 215, AcA, 1.8 ms, α ~100% / β⁻ $5\cdot10^{-4}$%	At 215, ~100 µs, α							
211		Pb 211, AcB, 36.1 m, β⁻	Bi 211, AcC, 2.15 m, α 99.68% / β⁻ 0.32%	Po 211, AcC′, 0.52 s, α								
207	Tl 207, AcC″, 4.8 m, β⁻	Pb 207, AcD, stable										

Table 11: Natural radioactive familiy of ^{235}U [51].

- Uranium-lead is the most refined of the radiometric dating schemes, with a age range of about 1 million years to over 4.5 billion years, and with precisions in the $0.1-1$ percent range [32].

- The decay constants of ^{235}U and ^{238}U are well known with the accuracy within one-tenth of a percent-range, whereas the decay constants used for the dating of other radioactive elements are usually known only with an accuracy at the percent level.

Two disadvantages of this method are:

- The analyzed rocks usually have unknown and complex history (disturbance in the U-Pb system).

- Potential continuous lead loss.

The explanation of the mathematics of this process follows.
'p' is for present, 'i' is for initial, so for example ^{206}Pb$_p$ gives the present number of ^{206}Pb isotopes and so forth. Equation 22 can be written

for ^{206}Pb

$$^{206}\text{Pb}_p = ^{206}\text{Pb}_i + ^{238}\text{U}_p \cdot (e^{\lambda_{238} t} - 1) \tag{23}$$

and for ^{207}Pb

$$^{207}\text{Pb}_p = ^{207}\text{Pb}_i + ^{235}\text{U}_p \cdot (e^{\lambda_{235} t} - 1) \tag{24}$$

where ^{206}Pb respectively ^{207}Pb means number of atoms N of ^{206}Pb rrespectively ^{207}Pb, λ_{238} is $1.55125 \cdot 10^{-10}$ y^{-1}, and λ_{235} is $9.8485 \cdot 10^{-10}$y^{-1}. In a second step, these equations are divided by the amount of ^{204}Pb (Equations 25 and 26), because the isotope ^{204}Pb is the only not radiogenic nuclide (and is treated as a stable reference isotope). The initial ^{238}U/^{204}Pb ratio is called μ. The ratio ^{238}U/^{235}U is given and known at any time in the Earth history and today is 137.88.

$$\left(\frac{^{206}\text{Pb}}{^{204}\text{Pb}}\right)_p = \left(\frac{^{206}\text{Pb}}{^{204}\text{Pb}}\right)_i + \mu \left(e^{\lambda_{238} t} - 1\right) \tag{25}$$

and

$$\left(\frac{^{207}\text{Pb}}{^{204}\text{Pb}}\right)_p = \left(\frac{^{207}\text{Pb}}{^{204}\text{Pb}}\right)_i + \frac{\mu}{137.88} \left(e^{\lambda_{235} t} - 1\right) \tag{26}$$

The equations above can be rearranged by subtracting the initial ratio from both sides

$$\left(\frac{^{206}\text{Pb}}{^{204}\text{Pb}}\right)_p - \left(\frac{^{206}\text{Pb}}{^{204}\text{Pb}}\right)_i = \mu \left(e^{\lambda_{238} t} - 1\right) \tag{27}$$

and

$$\left(\frac{^{207}\text{Pb}}{^{204}\text{Pb}}\right)_p - \left(\frac{^{207}\text{Pb}}{^{204}\text{Pb}}\right)_i = \frac{\mu}{137.88} \left(e^{\lambda_{235} t} - 1\right) \tag{28}$$
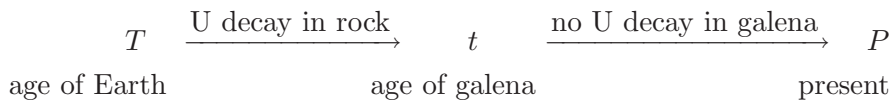
50

Dividing equation 28 by equation 27 to eliminate μ results in:

$$\frac{\left(\frac{^{207}\text{Pb}}{^{204}\text{Pb}}\right)_p - \left(\frac{^{207}\text{Pb}}{^{204}\text{Pb}}\right)_i}{\left(\frac{^{206}\text{Pb}}{^{204}\text{Pb}}\right)_p - \left(\frac{^{206}\text{Pb}}{^{204}\text{Pb}}\right)_i} = \frac{\left(e^{\lambda_{235}t} - 1\right)}{137.88\left(e^{\lambda_{238}t} - 1\right)} \tag{29}$$

If the present-day Pb isotope composition of different samples from the same mine are plotted ($^{207}\text{Pb}/^{204}\text{Pb}$ versus $^{206}\text{Pb}/^{204}\text{Pb}$, i.e., the left-hand side of equation 29), they should form a straight-line array, provided that they have remained in a closed system. The slope of this array, termed an 'isochron'[1], depends only on t, and does not require any knowledge of the U and Pb concentrations in the samples. Equation 29 cannot be solved analytically for t (it is a transcendental equation), however there are different possibilities of solving this problem numerically: one can use the Isoplot (Excel-based program by K.R. Ludwig, Berkeley Geochronology Center) or write an approximating programme (e.g. in MatLab) using simple minimization algorithms (that generally will converge to a high degree of accuracy after a few iterations).

4.1.2 Galena: Pb-Pb age calculation

The mineral galena is generally accepted for Pb-Pb age determination. The speciality of galena is that it contains no U anymore (in contrast to e.g. zircon), so there is no problem regarding U loss. Since there is no decay of U in the galena, its age is measured not directly back from the present, but from the formation of the Earth until the isolation of the galena as mineral. This model (conceived by Holmes (1946) and Houtermans (1946)) for terrestrial Pb isotope evolution may be summarized as follows:

$$T \xrightarrow{\text{U decay in rock}} t \xrightarrow{\text{no U decay in galena}} P$$

age of Earth   age of galena   present

The assumptions on which the Holmes-Houtermans model is based:

1. Originally, the Earth was fluid and homogenous.

---

[1]Isochron is the line in a diagram whose slope depends only on t. For instance, the slope of the correlation line on a plot of $^{207}\text{Pb}/^{204}\text{Pb}$ versus $^{206}\text{Pb}/^{204}\text{Pb}$ is an isochron. The notion of isochron was first introduced by Houtermans in 1947.

2. At that time U, Th and Pb were uniformly distributed.

3. The isotopic composition of the primeval Pb was everywhere the same.

4. Subsequently, the Earth became solid, small regional differences arose in the U/Pb ratio.

5. In any given region, the U/Pb ratio changed only as a result of radioactive decay of U to Pb.

6. At the time of formation of a common Pb mineral, such as galena, the Pb was separated from U and Th and its isotopic composition has remained the same since separation and thus representative of the ^{235}U/^{238}U ratio of that time.

The Holmes-Houtermans model accounts for the isotopic composition of any given sample of common Pb in terms of a single-stage history. It assumes that radiogenic Pb is produced by decay of U and Th in the source regions and that the resulting Pb (primeval plus radiogenic) is later separated from its parents and incorporated into ore deposits as galena. Given this model, the basic decay equation for ^{235}U-^{207}Pb is:

$$^{207}\text{Pb}_t = ^{207}\text{Pb}_T + ^{235}\text{U}(e^{\lambda_{235}T} - e^{\lambda_{235}t}) \tag{30}$$

where the Pb isotope composition at time T represents the composition of the solar nebula; that is the primordial composition of the Earth, best represented by Pb-isotope ratios of Canyon Diablo troilite (C.D.); t represents the present-day compsotion, since galena incorporates no U, it can be indicated with 'P'(for present). Each term is next divided through by ^{204}Pb and rearranged. The same procedure is applied to the corresponding equation for ^{206}Pb to yield:

$$\left(\frac{^{207}\text{Pb}}{^{204}\text{Pb}}\right)_P - \left(\frac{^{207}\text{Pb}}{^{204}\text{Pb}}\right)_T = \frac{^{235}\text{U}}{^{204}\text{Pb}}(e^{\lambda_{235}T} - e^{\lambda_{235}t}) \tag{31}$$

$$\left(\frac{^{206}\text{Pb}}{^{204}\text{Pb}}\right)_P - \left(\frac{^{206}\text{Pb}}{^{204}\text{Pb}}\right)_T = \frac{^{238}\text{U}}{^{204}\text{Pb}}(e^{\lambda_{238}T} - e^{\lambda_{238}t}) \tag{32}$$

by dividing the equation 31 by the equation 32 one gets an equation as follows:

$$\frac{\left(\frac{^{207}\text{Pb}}{^{204}\text{Pb}}\right)_P - \left(\frac{^{207}\text{Pb}}{^{204}\text{Pb}}\right)_{C.D.}}{\left(\frac{^{206}\text{Pb}}{^{204}\text{Pb}}\right)_P - \left(\frac{^{206}\text{Pb}}{^{204}\text{Pb}}\right)_{C.D.}} = \frac{(e^{\lambda_{235}T} - e^{\lambda_{235}t})}{137.88(e^{\lambda_{238}T} - e^{\lambda_{238}t})} \tag{33}$$

If the slope ratios on the left-hand side of the equation represent a sample extracted from the mantle at time t, then the term on the right-hand

side corresponds to the slope of an isochron line.

A growth curve is then constructed for the galena source, which runs from the primordial Pb composition to that of the analyzed galena, and is calibrated for different values of t. The major problem encountered with Holmes-Houtermans model was that as more galenas were analyzed they were found to scatter more and more widely on the Pb-Pb isochron diagram (Fig. 31).
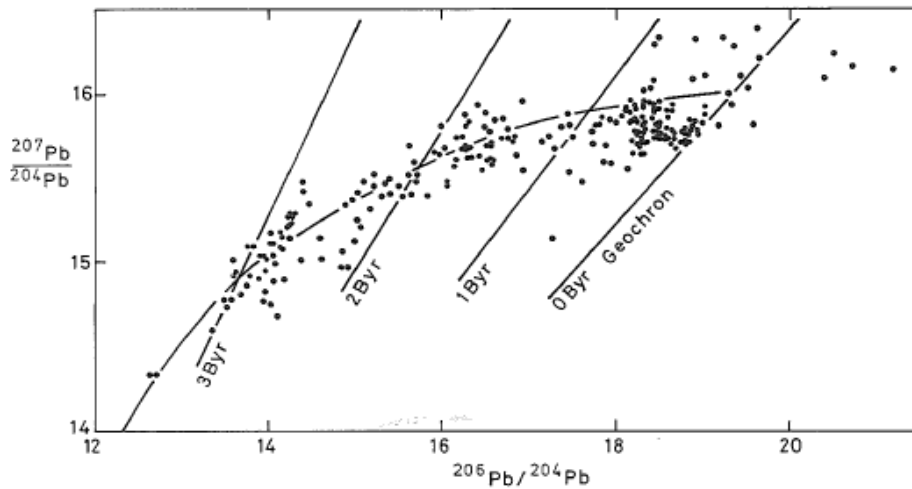

Figure 31: Pb-Pb isochron diagram showing a compilation of many analyzed galenas from different environments [47].

The discrepancy between the single-stage Pb dates of many ore deposits and their ages, as determined by other isotopic or geologic methods, requires a refinement of the Pb evolution model. Stacey and Kramers (1975) developed a two-stage model in which the evolution of Pb started with primordial isotope ratios 4.57 Ga ago. At a more recent date T', the U/Pb ratio of the reservoir was changed by geochemical differentiation and then remained constant to the present. Stacey and Kramers (1975) used Canyon Diablo Pb and the average of modern Pb (from a mixture of manganese modules, ocean sediments and island arc rocks) to define the ends of a composite growth curve [29]. In this model, Pb evolved between 4.57 Ga and 3.70 Ga in a reservoir having uniform $^{238}U/^{204}Pb$ (μ) and $^{232}Th/^{204}Pb$ (ω) ratios of 7.192 and 32.208, respectively. At a time of 3.70 Ga, the values of μ and ω were changed by geochemical differentiation to 9.735 and 36.837, respectively. Subsequently, the reservoir remained undisturbed until the present. Here are the parameters for the two-stage Pb evolution model of Stacey and Kramers (1975):

	Time, Ga	$\frac{^{206}Pb}{^{204}Pb}$	$\frac{^{207}Pb}{^{204}Pb}$	$\frac{^{208}Pb}{^{204}Pb}$	μ	ω
Start, Stage 1 (C.D)	4.57	9.307	10.294	29.476	7.192	32.208
Start, Stage 2	3.70	11.152	12.998	31.230	9.735	36.837
Present	0	18.700	15.628	38.630	9.735	36.837

Table 12: Parameters for the two-stage Pb evolution model of Stacey and Kramers [52].

For the Pb daughters of U, whose evolution happened after Stacey and Kramers model, the equation is:

$$\frac{\left(\frac{^{207}\text{Pb}}{^{204}\text{Pb}}\right) - 12.998}{\left(\frac{^{206}\text{Pb}}{^{204}\text{Pb}}\right) - 11.152} = \frac{(e^{\lambda_{235}T'} - e^{\lambda_{235}t})}{137.88 \cdot (e^{\lambda_{238}T'} - e^{\lambda_{238}t})} \tag{34}$$

where T'=3.70·10^9 years is the starting time of the second stage of Pb evolution. Equation 34 may be used to date common leads that satisfy the following conditions:

1. This leads evolved from primordial lead between 4.57 and 3.70 Ga in a uniform reservoir having μ=7.192 and ω=32.208.

2. At 3.70 Ga, the μ and ω values of the reservoir were changed but remained constant until the Present except for decay of U and Th to Pb.

3. Lead was removed from the reservoir at some time t and was incorporated into a common Pb mineral, e.g. galena or zircon.

4. After separation from the reservoir, the isotopic composition of the Pb was not changed by mixing with other leads or by additions of radiogenic Pb formed by decay of U and Th.

Due to the mobility of Pb during crustal processes, it is difficult to develop an *a priori* criteria to recognize galenas which will fit the conformable Pb evolution model. Therefore, the galena Pb-Pb method is largely discredited as a dating tool. Nevertheless, this method may provide powerful constraints to the evolution of different celestial bodies such as the evolution of the martian moons [22], [29].

Pb is one of the highly volatile elements. This means that different processes on planets and meteorite parent bodies, which include a high temperature (evaporation and/or condensation) will lead to elemental and/or isotopic depletion in different volatile elements including Pb in bulk composition of these bodies relative to bulk Solar System composition. The

Sample	Isotopes	$\frac{Pb^{206}}{Pb^{204}}$	$\frac{Pb^{207}}{Pb^{204}}$	$\frac{Pb^{208}}{Pb^{204}}$
Be 17	Data 1963 TIMS LMS	18.52 18.406	15.78 15.654	38.80 38.423
Be 25	Data 1963 TIMS LMS	12.73 12.665	14.32 14.236	32.65 32.490
Be 36	Data 1963 TIMS LMS	18.13 17.997	15.78 15.639	38.17 37.729
Be 62	Data 1963 TIMS LMS	15.72 15.595	15.50 15.317	35.74 35.260
Be 75	Data 1963 TIMS LMS	19.10 19.047	15.73 15.677	39.20 39.114
Be 96	Data 1963 TIMS LMS	17.48 17.305	15.92 15.701	37.26 36.651

absence of isotopic fractionation in a volatile element-depleted condensed phase is a measure of the degree to which the system maintained thermodynamic equilibrium. The degree of the depletion could provide the hints for the mechanisms (temperature- and pressure conditions, timescale) of volatility fractionation and thus, points to the conditions the parent bodies were changed at. [28]

4.2   IR-measurements (Nd:YAG)

4.3   UV-measurements (Nd:YAG)

4.4   Elemental analysis (trace elements)

4.5   Data interpretation

To evaluate the results of LMS, we had the opportunity to do the same measurements with the TIMS instrument (Prof. K. Mezger, Geology department, University of Bern). This gave us the additional

4.6   Summary

Conclusions

The Phobos-Grunt spacecraft is on the way to its missions goal. The mission success will depend on different factors.

List of Tables

List of Figures

References

[1] http://www.esa.int

[2] J. H. Shirley and R. W. Fairbridge. *Encyclopedia of Planetary Sciences, p. 572−575.* Chapman & Hall, 1st edition, 1997.

[3] A. V. Ivanov. *Is the Kaidun Meteorite a Sample from Phobos?* 2003.

[4] N. Thomas, R. Stelter, A. Ivanov, N. T. Bridges, K. E. Herkenhoff, A. S. McEwen, *Spectral heterogeneity on Phobos and Deimos: HiRISE observations and comparisons to Mars Pathfinder results,* Planetary and Space Science 59 (2011) 1281−1292.

[5] http://moons-phobos.generalanswers.org/

[6] G. G. Managadze, P. Wurz, R. Z. Sagdeev, A. E. Chumikov, M. Tulej, M. Iakovleva, N. G. Managadze, and A. L. Bondarenko. *Study of the Main Geochemical Characteristics of Phobos' Regolith Using Laser Time-of-Flight Mass Spectrometry* 2010.

[7] A. S. Rivkin, R. H. Brown, D. E. Trilling, J. F. Bell, J. H. Plassmann, *Near-infrared spectrophotometry of Phobos and Deimos,* Icarus 156 (2002), 64−75.

[8] M. Giuranna, T. L. Roush, T .Duxbury, R. C. Hogan, C. Carli, A. Geminale, V. Formisano, *Compositional interpretation of PFS/MEx and TES/MGS thermal infrared spectra of Phobos* Planetary and Space Science 59, 1308−1325, 2011.

[9] S. Murchie, S. Erarde, *Spectral Properties and Heterogeneity of Phobos from Measurements by Phobos 2,* Icarus 123, 63−86, 1996.

[10] R. A. Craddock *Are Phobos and Deimos the result of a giant impact?* Icarus 211, 1150−1161, 2011.

[11] A. Cazenave, A. Dobrovolskis, B. Lago, *Orbital history of the Martian satellites with inferences on their origin,* Icarus 44, 730−744, 1981.

[12] J. A. Burns in: H. H. Kieffer, B. M. Jakosky, C. W. Snyder, M. S.Matthews *Mars, pp 1283−1301.* The University of Arizona Press. 1992.

[13] http://www.icp-ms.de/wasist.html.

[14] J. Salisbury, D. D'Aria, E. Jarosewich, *Midinfrared (2.5−13.5 μm) reflectance spectra of powdered stony meteorites,* Icarus 92, 280−297, 1991.

[15] P. Rosenblatt *The origin of the Martian moons revisited* Astron Astrophys Rev 2011.

[16] L. Dones, S. Tremaine, *Why does the Earth spin forward?* Science 259, 350−354, 1993.

[17] galspace.spb.ru.

[18] http://northernanalytical.com/tech3.htm

[19] http://www.olympus.de/microscopy/4427_microglossary.cfm?buchstabe =1&app_id=135.

[20] http://www.webelements.com/webelements/elements/text/xe/isot.html.

[21] *Melles Griot, Optics Catalogue 2002.* http://www.mellesgriot.com.

[22] *Geol. 656 Isotope Geochemistry.* http://www.geo.cornell.edu/geology/ classes/Geo656/656notes03/656re04.pdf, 2003.

[23] B. A. Mamyrin, V. I. Karataev, D. V. Shmikk, V. A. Zagulin. *The mass-reflectron, a new nonmagnetic time-of-flight mass spectrometer with high resolution.* Sov. Phys. JETP, 37, 45, 1973.

[24] D. Abplanalp. *Kleinstmassenspektrometer für planetologische Untersuchungen.* Diplom thesis, University of Bern, 2005.

[25] M. Iakovleva. *Preparation for measurements of the surface composition of Phobos.* Universität Bern, 2007.

[26] R. J. Cotter. *Time-of-Flight Mass Spectrometry, p. 47−53,* ACS Professional Reference Books, 1st edition, 1997.

[27] R. R. Parrish, S. R. Noble. *Zircon U-Th-Pb Geochronology by Isotope Dilution - Thermal Ionization Mass Spectrometry (ID-TIMS).* Reviews in Mineralogy & Geochemistry , Volume 53, p. 183−213, 2003.

[28] A. M. Davis and F. M. Richter, Editors-in-Chief: Heinrich D. Holland and Karl K. Turekian, Treatise on Geochemistry, *Condensation and Evaporation of Solar System Materials.* Elsevier Ltd. 2004.

[29] A. P. Dickin. *Radiogenic Isotope Geology, p. 104−132.* Cambridge University Press, 1st edition, 1995.

[30] H. H. Kieffer, B. M. Jakosky, C. W. Snyder, M. S.Matthews *Mars, p. 1257−1301.* The University of Arizona Press. 1992.

[31] *Inorganic Mass Spectrometry* Edited by F. Adams, R. Gijbels, R. Van Grieken. G. Ramendik, Spark Source Mass Spectrometry, p. 319. A Wiley-Interscience Publication. 1988.

[32] *Zircon U-Th-Pb geochronology by isotope dilution: Thermal ionization mass spectrometry (ID-TIMS)* R. R. Parrish, S. R.Noble, Reviews in Mineralogy and Geochemistry, p. 183−213. Mineralogical Society of America. 2003.

[33] *Inorganic Mass Spectrometry* Edited by F. Adams, R. Gijbels, R. Van Grieken. K. G.Heumann, Isotope Dilution Mass Scpectrometry, p. 17. A Wiley-Interscience Publication. 1988.

[34] Edited by A. Vertes., R. Gijbels and F. Adams. *Laser Ionization Mass Analysis* G. G. Managadze and I. Yu. Shutyaev, Exotic instruments and applications of laser ionization mass spectrometry in space research, pp.519-524, John Wiley & Sons, Inc. 1993.

[35] Edited by A. Vertes., R. Gijbels and F. Adams. *Laser Ionization Mass Analysis* L. Moenke-Blankenburg, The High Laser Irradiance Regime, Solid Sampling For Analysis By Laser Ablation, p. 433. John Wiley & Sons, Inc. 1993.

[36] J. H. Gross. *Mass spectrometry : a textbook / Jürgen H. Gross, p. 110−120.* Berlin : Springer, 2004.

[37] http://www.laspace.ru/rus/phobos.php.

[38] H. H. Kieffer, P. Thomas, et al., and J. A. Burns. *Mars. Satellites of Mars: geologic history. Origin of martian moons: contradictory clues, p. 1256−1302.* The University of Arizona Press, 5th edition, 1992.

[39] M. V. Klein and T. E. Furtak. *Optics, p. 99−148.* John Wiley and Sons.

[40] H. W. Köhler. *Der Mars, p. 40−57, Bericht über einen Nachbarplaneten.* Vieweg, 1st edition, 1978.

[41] N. G. Managadze and G. G. Managadze. *The quantitative nonreference express-analysis of some alloys with a time-of-flight laser mass spectrometer.*

[42] L. M. Zelenyi, A. V. Zakharov, G. M. Polischuk, and M. B. Martynov, *Project of the Mission to Phobos.* Solar System Research (44), pp. 15−25, 2010.

[43] A. Balogh, M. Bird, L. Blomberg, P. Bochsler, J.-L. Bougeret, J. Brückner, L. Iess, J. Buest, Y. Langevin, A. Milani, J.-A. Sauvaud, W. Schmidt, T. Spohn, R. von Steiger, N. Thomas, K. Torkar, H. WŠnke and P. Wurz. *BepiColombo − An interdisciplinary cornersone mission to the planet Mercury.* ESA-SCI, Noordwijk, The Netherlands, European Space Agency, 2000.

[44] J. van Casteren, M. Novara, R. Best, H. Hayakaw, P. Ferri. *The BepiColombo Mission.* Planetary Space Science, submitted for publication.

[45] G. G. Managadze, P. Wurz, R. Z. Sagdeev, A. E. Chumikov, M. Tulej, M. Iakovleva, N. G. Managadze, A. L. Bondarenko, *Study of the Main Geochemical Characteristics of Phobos' Regolith Using Laser Time-of-Flight Mass Spectrometry* Astronomicheskii Vestnik, 2010, Vol. 44, No. 5, pp. 405−413

[46] D. Rothery, L. Marinangeli, M. Anand, J. Carpenter, U. Christensen, I. A. Crawford, M. C. De Sanctis, E. Mazzotta Epifani, S. Erard, A. Frigeri, G. Fraser, E. Hauber, J. Helbert, H. Hiesinger, K. Joy, Y. Langevin, M. Massironi, A. Milillo, I. Mitrofanov, K. Muinonen, J. Näränen, C. Pauselli, Ph. Potts, J. Warell, P. Wurz, *Mercury's surface and composition to be studied by BebiColombo* Planetary and Space Science 58 (2010) 21−39.

[47] R.L. Stanton and R.D. Russell, *Anomalous leads and the emplacement of lead sulphide ores (1959).* Econ. Geol. 54, 588−607

[48] T. Mayer-Kuckuk. *Kernphysik, eine Einführung, p. 73−74.* B. G. Teubner GmbH, 7th edition, 2002.

[49] F. J. McClung and R. W. Hellwarth. *Giant optical pulsations from ruby, p. 828−829.* Journal of Applied Physics 33(3), 1962.

[50] R. O. Norton. *The Cambridge encyclopedia of meteorites, p. 82−83.* Cambridge University Press, 2002.

[51] G. Pennig, H. Klewe-Nebenius, and W. Seelmann-Eggebert. *Karlsruher Nuklidkarte, p. 24.* Druckhaus Haberbeck GmbH, 6th edition, 1998.

[52] J. S. Stacey, J. D. Kramers. *Approximation of terrestrial lead isotope evolution by a two-stage model.* Earth Planet.Sci. Letters, 26, 207−221, 1998.

[53] C. R. Phipps and R. W. Dreyfus. *Chemical Analysis Series, chapter 4: The high laser irradiance regime. Laser Ionization Mass Analysis, p. 369−431*, volume 124. John Wiley and Sons, Inc., 1993.

[54] U. Rohner. *Development of highly miniaturised laser-mass-spectrometer for the in situ analysis of planetary surfaces,* PhD Thesis, Universität Bern, 2004.

[55] W. E. Stephens. *A Pulsed Mass Spectrometer With Time Dispersion, p. 691.* Phys. Rev. 69, 1946.

[56] O. Svelto. *Principles of Lasers, p. 313.* 4th edition, 1998.

[57] H. P. Weber. *Experimentelle Optik Vorlesungsskript, Institut für angewandte Physik, p. 97−111.* Universität Bern, 1999.

[58] http://www.photonis.com/

[59] S. Meyer *Performance Studies of a Time-Of-Flight Mass Spectrometer for the in-situ Analysis of Planetary Surfaces* Bachelor Thesis, August 2011

[60] T. P. Andert, P. Rosentblatt, M. P"atzold, B. H"ausler, V. Dehant, G. L.Tyler and J. C.Marty *Precise mass determination and the nature of Phobos* Geophysical Research Letters, Vol.37, 2010.

[61] D. S. McKay, J. L. Carter, W. W. Boles, C. C. Allen, and J. H. Allton, *JSC-1: A New Lunar Soil Simulant* Engineering, Construction, and Operations in Space IV American Society of Civil Engineers, pp. 857-866, 1994.

[62] W. C. Wiley, I. H. MacLaren, Rev. Sci. Instr., 26, 1150, 1955